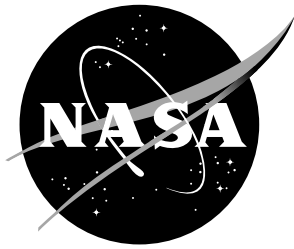# Analysis of Open Hole Compression Specimens Using the CompDam Continuum Damage Mechanics Model

Andrew C. Bergan
Langley Research Center, Hampton, Virginia

Sarah J. Murphy
The Boeing Company, Huntsville, Alabama

Lillian F. Miles
The Boeing Company, Charleston, South Carolina

NASA STI Program...in Profile

Since its founding, NASA has been dedicated to the advancement of aeronautics and space science. The NASA scientific and technical information (STI) program plays a key part in helping NASA maintain this important role.

The NASA STI Program operates under the auspices of the Agency Chief Information Officer. It collects, organizes, provides for archiving, and disseminates NASA's STI. The NASA STI Program provides access to the NASA Aeronautics and Space Database and its public interface, the NASA Technical Report Server, thus providing one of the largest collection of aeronautical and space science STI in the world. Results are published in both non-NASA channels and by NASA in the NASA STI Report Series, which includes the following report types:

- TECHNICAL PUBLICATION. Reports of completed research or a major significant phase of research that present the results of NASA programs and include extensive data or theoretical analysis. Includes compilations of significant scientific and technical data and information deemed to be of continuing reference value. NASA counterpart of peer-reviewed formal professional papers, but having less stringent limitations on manuscript length and extent of graphic presentations.

- TECHNICAL MEMORANDUM. Scientific and technical findings that are preliminary or of specialized interest, e.g., quick release reports, working papers, and bibliographies that contain minimal annotation. Does not contain extensive analysis.

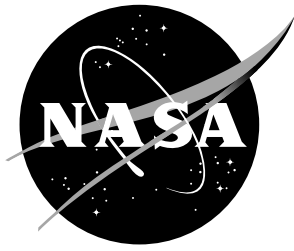- CONTRACTOR REPORT. Scientific and technical findings by NASA-sponsored contractors and grantees.

- CONFERENCE PUBLICATION. Collected papers from scientific and technical conferences, symposia, seminars, or other meetings sponsored or co-sponsored by NASA.

- SPECIAL PUBLICATION. Scientific, technical, or historical information from NASA programs, projects, and missions, often concerned with subjects having substantial public interest.

- TECHNICAL TRANSLATION. English-language translations of foreign scientific and technical material pertinent to NASA's mission.

Specialized services also include organizing and publishing research results, distributing specialized research announcements and feeds, providing information desk and personal search support, and enabling data exchange services.

For more information about the NASA STI Program, see the following:

- Access the NASA STI program home page at http://www.sti.nasa.gov

- E-mail your question to help@sti.nasa.gov

- Phone the NASA STI Information Desk at 757-864-9658

- Write to:
  NASA STI Information Desk
  Mail Stop 148
  NASA Langley Research Center
  Hampton, VA 23681-2199

Analysis of Open Hole Compression Specimens Using the CompDam Continuum Damage Mechanics Model

Andrew C. Bergan
Langley Research Center, Hampton, Virginia

Sarah J. Murphy
The Boeing Company, Huntsville, Alabama

Lillian F. Miles
The Boeing Company, Charleston, South Carolina

November 2020

Acknowledgments

Available from:

NASA STI Program / Mail Stop 148
NASA Langley Research Center
Hampton, VA 23681-2199
Fax: 757-864-6500

Abstract

This report documents a validation study on the standard Open Hole Compression (OHC) laminate test specimen conducted as part of the NASA Advanced Composites Project (ACP). Tests were conducted on OHC specimens with hard, quasi-isotropic, and soft layups using digital image correlation and X-Ray computed tomography to capture the structural response and damage evolution. Progressive damage models were constructed for use with the CompDam continuum damage mechanics code following the best practices established during the ACP. Detailed interrogation of the analysis results and comparison with experimental measurements provide a basis for assessing the capability of the modeling approach for OHC. The structural response is found to be captured well, with strengths predicted within 3% of the experimental values for hard and quasi-isotropic laminates. In the soft laminate, the model predicts failure to be more brittle than the nonlinear, ductile response that was measured. Damage states extracted from the models at the same load level as test measurements are overlaid to show directly the similarities and differences between test and analysis results. Studying the damage evolution predicted by the analysis reveals that the failure process is a competition between fiber damage and delamination/sub-laminate buckling, with fiber damage dominating the collapse in the hard laminate and sub-laminate buckling governing in the soft laminate. Finally, a series of parametric studies varying numerical solution parameters (mesh size, mass scaling) and physical properties (fiber direction compressive strength and toughness) reveal sensitivities and deficiencies of the model. To the authors' knowledge, this study is the first for OHC specimens to include detailed evaluation of damage mode interactions, direct overlay of predicted and measured damage states, and sensitivity of the predicted results to difficult-to-measure fiber direction material properties.

1 Introduction

The Open Hole Compression (OHC) specimen is a common coupon used to obtain design allowables for composite aerospace structures. The OHC specimen is also a valuable configuration for evaluating the capability of progressive damage and failure analysis (PDFA) techniques with regard to compression failures since a complex network of matrix cracking, delamination, and fiber damage develop and then precipitate catastrophic failure. The damage events are numerous, discrete, and are often competing mechanisms that eventually result in two-piece failure. As a result, to the authors' knowledge, no model is able to predict accurately the structural response and associated damage across a wide range of OHC specimen configurations.

The hallmark of a successful PDFA model is that it predicts a laminate-level structural response resulting from damage onset and propagation using material properties measured at the ply or constituent level. In general, evaluating the capability of PDFA techniques involves accurately capturing stiffness, strength, and damage progression. Although capturing the stiffness and strength is necessary, focusing only on these two objectives omits validation of underlying progression of the damage mechanisms, which is the mechanism by which the structural response is predicted in PDFA. Therefore, it can only be expected that a PDFA approach is predictive when it captures not only the stiffness and strength, but also the damage progression observed in validation tests. Therefore, a detailed experimentally-informed understanding of the damage progression behavior is needed.

An early account of the sequence of events leading to failure in OHC specimens with different layups is given by Waas et al. [1] based on a series of experiments using holographic interferometry to identify local out-of-plane displacements and photomicrography of the hole surface. They report failure is initiated by fiber kinking in the 0° plies at the hole surface, followed by extensive delamination and cracking that propagates until the delaminated area reaches a critical size corresponding to sufficient loss of flexural stiffness for collapse of the specimen. Through visual observations on the hole surface and out-of-plane deformations on the face of the specimens recorded through the loading sequence, Waas et al. infer that fiber kinking onset occurs instantaneously. When the specimen does not collapse at this point, the fiber kinking subsequently propagates stably under increasing load. In addition, the authors report that the failure is more brittle in hard laminates with a large percentage of 0° plies and relatively ductile in soft laminates with few 0° plies. Several other experimental studies have reported similar findings regarding the damage modes and sequence of events [2–5]. In Suemasu et al. 2012 [6], observations from a high-speed camera were used to conclude that the final collapse in quasi-isotropic specimens is due to delamination propagation and sub-laminate buckling. Other experimental studies have evaluated size effects and ply sequencing effects showing the layup can have a significant effect on the observed notch sensitivity and failure modes [2, 4, 7]. Xu et al. [8] found similar damage patterns in OHC and center notch specimens. Examining the center notch specimens with X-Ray computed tomography (CT), they reported competition between matrix cracking and fiber kinking, where plies without matrix cracks tended to kink earlier than plies with matrix cracks, apparently a result of the matrix cracks blunting the notch tip stress

concentration. Leopold et al. [9] reported that the 0° ply location through the laminate thickness and to a lesser extent ply thickness, were correlated with different fiber kinking characteristics and therefore different strengths. In cases with thin 0° plies near the mid-plane of the laminate (i.e., better supported by adjacent plies), fiber kinking onset was delayed. Based on these experimental observations, it can be concluded that it is necessary to predict the interaction of fiber kinking, matrix cracking, and delamination accurately in order to have a general PDFA modeling capability suitable for a range of OHC configurations.

Several researchers have made progress toward establishing PDFA models for OHC. Iarve et al. [10] showed the importance of predicting matrix splitting cracks accurately in order to account for the consequent reduction in axial strain concentration next to the hole. Lee and Soutis [11] also examined splitting and found that splitting is more prevalent in thick plies, and that extensive splitting cracks make the OHC less notch sensitive by blunting the stress concentration. Another experimentally observed aspect of the failure process, unstable fiber kinking onset followed by stable propagation, was investigated in [5]. By systematically reducing element stiffness to 1/10 the original values, it was demonstrated that the stress redistribution that occurs after fiber kinking causes fiber kinking to initiate unstably to a minimum size after which stable growth can occur. Davidson et al. [12] presented a variety of different modeling approaches with increasing fidelity and compared the results to show where higher fidelity models are required. While the experimental evidence points toward fiber kinking as the source of local delamination and out-of-plane deformations near the hole, some researchers have been able to reproduce similar local deformations without considering the kinematics of fiber kinking [13, 14].

Despite these advances in modeling, OHC remains a challenging problem for PDFA as has been illustrated in various analysis capability evaluations [15, 16]. In the recent Air Force Research Lab Tech Scout program [15], the accuracy of OHC predictions for strength was 14.2% pretest and improved to 6.4% after posttest adjustments. In the world-wide failure exercise III [16], strength predictions from several theories for OHC in quasi-isotropic laminates varied by almost a factor of two.

Two explanations are offered for the deficiency in existing model performance. First, more systematic comparison of the damage evolution observed in tests and predicted by analysis is needed. It is clear from test observations that the OHC failure process includes multiple interacting damage modes that evolve under load. Therefore, a thorough documentation of the damage states from experimentally detectable damage onset up to unstable collapse is needed. By quantitative comparison of predicted and measured damage states, more clarity can be obtained as to where models are successful and deficient. Second, most models require strength and toughness material properties for fiber compression (fiber kinking), for which no consensus has been established on test methods for characterization.

The objective of this report is to document the findings of a recent OHC validation activity conducted as part of the NASA Advanced Composites Project (ACP). One aspect of the ACP was to verify and validate PDFA methods for application to selected structural components. As part of a larger verification and validation

4

effort, this study on OHC benefits from a consistent and complete set of material properties [17], numerous verification studies [18–20], and lessons learned from PDFA for other structural configurations [21–26]. The PDFA method used in this study is the continuum damage mechanics (CDM) code developed at NASA Langley Research Center, CompDam [27]. CompDam is a research code developed to help improve understanding of material modeling requirements for CDM methods. The code has multiple methods and several different optional features for modeling damage. The most basic capability of the code uses the deformation gradient decomposition method [28] to model matrix cracks and a trilinear constitutive law to model fiber damage. The goal of this study is to establish the predictive capabilities of the CompDam code in its baseline configuration, to identify technical gaps, and to inform future development priorities. Therefore, ongoing development capabilities such as inclined matrix cracks, shear nonlinearity, fiber nonlinearity, and fiber kinking were not used in this study.

OHC tests were conducted on three laminates. Digital image correlation (DIC) and X-Ray CT were used to quantify the damage states through the loading history. Posttest PDFA models were constructed with the continuum damage mechanics code CompDam, using the same practices as for the other modeling activities pursued in the ACP. To the authors' knowledge, this study is the first for the OHC configuration to include detailed evaluation of damage mode interactions, quantitative comparison of damage states, and sensitivity of the predicted results to difficult-to-measure fiber direction material properties.

This report is organized as follows. The experimental procedure and results are described in Section 2. The progressive damage analysis and finite element models are described in Section 3. The analysis results including structural response, damage evolution, and comparison with experimental measurements are discussed in Section 4. The sensitivity to selected numerical parameters and physical properties are reported in Section 5 and Section 6, respectively. Finally, the report is summarized with concluding remarks in Section 7.

2 Experiments

A series of OHC tests were performed in order to generate a set of data for evaluating the performance of different PDFA models. The test procedure and results are summarized in this section. The tests were conducted by The Boeing Company and the posttest X-Ray CT scans were conducted by NASA Langley.

2.1 Test procedure

The specimens were fabricated from 190 g/m^2 IM7/8552 unidirectional plies using hand layup and autoclave cure following the manufacturer's recommendations. The cured ply thickness was measured to be 0.183 mm on average. Pretest ultrasounds verified all test specimens were free of gross manufacturing defects. Test specimens were cut from three panels having the layups summarized in Table 1. The layups are a 24-ply quasi-isotropic laminate, a relatively soft laminate of 20 plies, and a
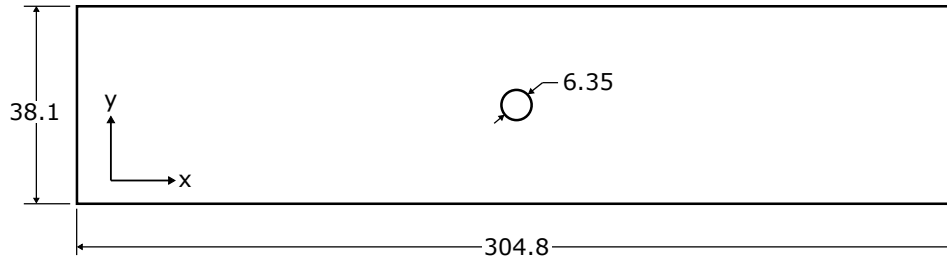
(a) Specimen layout (dimensions in mm).
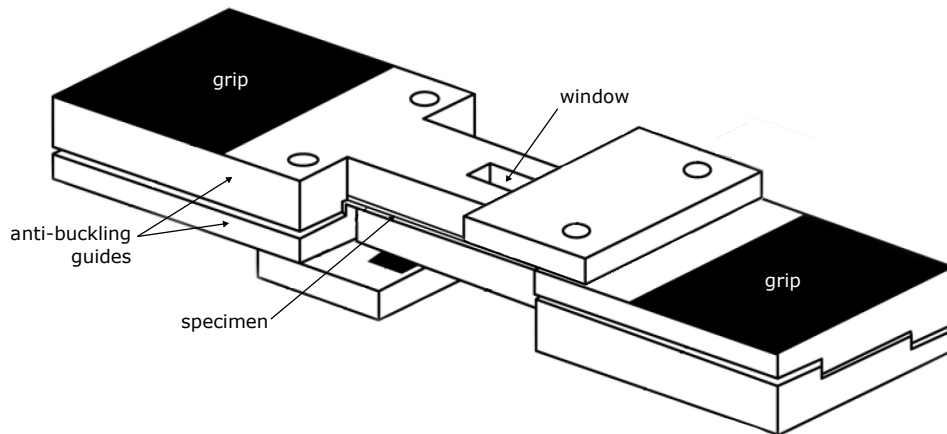
(b) OHC test fixture (adapted from [30]).

Figure 1: Schematics of specimen and OHC test fixture.

Table 1: OHC layups.

Designation	Stacking sequence	% plies $0/\pm 45/90$
Hard	$[(45/\text{-}45/0_2)_3]_s$	50/50/0
Quasi	$[(45/0/\text{-}45/90)_3]_s$	25/50/25
Soft	$[45/\text{-}45/0/45/\text{-}45/90/(45/\text{-}45)_2]_s$	10/80/10

relatively hard laminate of 24 plies. Three different laminates were used since damage progression is often very sensitive to the layup [29]. Therefore, while validating a PDFA model against a single layup is a useful exercise, it is not sufficient to generate confidence for engineering applications where a design space may include several layups. The particular layups selected were intended to be representative of the three classes of laminates and to encourage different damage evolution so as to challenge the models. The laminates are referred to herein as Hard, Quasi, and Soft.

The specimens were 304.8 mm long (L) by 38.1 mm wide (W) with a 6.35 mm diameter hole (d_h) in accordance with the ASTM standard [30] Procedure A and as shown in Figure 1a. The specimens were loaded using the standard OHC fixture shown in Figure 1b (constrains out-of-plane displacements) under a quasi-static loading with a prescribed displacement rate of 0.6 mm/min using a 245 kN load

frame. A 25.4 mm extensometer was centered across the hole and aligned with the loading axis to measure displacement during testing. Load and displacement data were recorded at 10 Hz.

A 3-D digital image correlation (DIC) system was used on one side of the specimen. The system used two 5 MP cameras set to view the specimen with a field of view of about 50 mm x 50 mm centered about the hole. Images were captured at 1 Hz and processed using ARAMIS software.

Five replicates were tested for each layup. The tests were conducted under room temperature ambient conditions. The first three test specimens for each layup were loaded monotonically to catastrophic failure following the standard test procedure. The average strength, $\sigma_{c,exp}$, was calculated from the first three tests. The fourth and fifth test specimens were loaded to 75% and 90% of $\sigma_{c,exp}$, respectively, and then unloaded for subsequent inspection via X-Ray CT. X-Ray CT scans were conducted using a resolution of 8 μm per voxel. The scan volume was roughly centered on the hole: 22 mm wide x 15 mm high x the laminate thickness.

2.2 Test results

Nominal stress vs. strain curves for all of the test specimens loaded to failure are shown in Figure 2. The nominal stress σ is the load divided by the original cross sectional area and the nominal strain ε is obtained from the axial extensometer. The results show excellent repeatability among the test replicates for each laminate. For each laminate, a dashed line shows the initial stiffness fit to the experimentally measured response from 0 to 100 MPa. A slight decrease in stiffness from the linear response is seen all cases, occurring well before peak load. The Hard and Quasi laminates exhibit a nearly linear response up to a sudden failure. The Soft specimens are also nearly linear initially up to an apparent damage onset load around 150 MPa, after which the specimens continue to sustain additional load, but with a lower stiffness and several small load drops up to the peak load. The nominal stress and strain pairs at which the 75% and 90% X-Ray CT scans were conducted are shown on the plot as 'x' and '+' symbols, respectively. The average stiffnesses E_{exp} (calculated from 0 to 100 MPa), strengths $\sigma_{c,exp}$, and strains-to-failure $\varepsilon_{c,exp}$ are summarized in Table 2. The square and triangle markers, gray in color, mark observations made from the DIC data and are discussed below.

The DIC system captured evidence of damage progression in all the tests. Selected frames from a representative replicate loaded to failure for each of the three layups are shown in Figure 3. The figure shows several frames of axial strain up

Table 2: Average measured stiffnesses, strengths, and strains-to-failure.

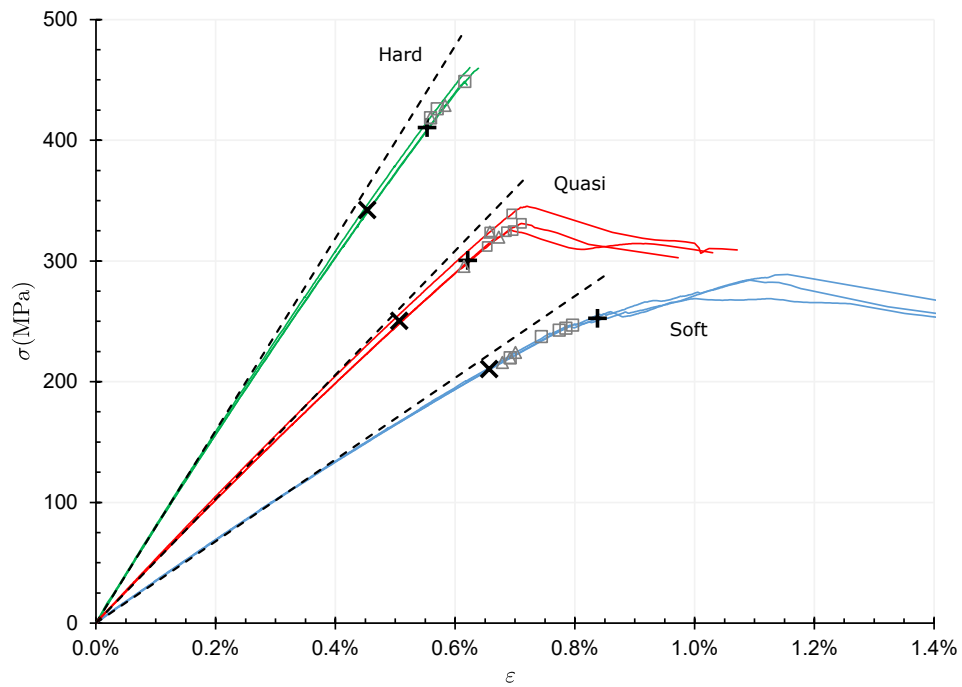| Layup	Stiffness E_{exp} [GPa]	Strength $\sigma_{c,exp}$ [MPa]	Strain-to-failure $\varepsilon_{c,exp}$ [%]
Hard	79.7	456.2	0.63
Quasi	51.4	334.0	0.71
Soft	33.9	280.5	1.12

7

Figure 2: Nominal stress vs. strain from the OHC tests for the three layups. The 'x' and '+' markers denote X-Ray CT scans and the open symbols denote points where damage was observed via DIC.

to the peak load and the final post-failure image from the Hard, Quasi, and Soft laminates in (a)–(f), (g)–(l), and (m)–(r), respectively. Each image shows a local region around the hole, as visible through the opening in the OHC test fixture. The loading direction is horizontal in these images and throughout the report (see the schematic in Figure 4c). The frame number is labeled f and the corresponding load normalized to the replicate's strength is labeled P for each image. The particular frames included in the figure were selected to show that the same set of events occurs in each layup, so the frame numbers and corresponding loads vary for each layup. The first frame shown in the figure for each layup ((a), (g), and (m)) is the last frame captured before damage is evident in the strain field. The contours are similar to each other in pattern and magnitudes. The second frame ((b), (h), and (n)) is the frame immediately following, which shows the first indication of damage in the strain field. In all three layups, the strain field shows evidence of local bending on one side of the hole, implying local delamination and sublaminate buckling. This pattern matches the results reported in [1] obtained using holographic interferometry. In [1] the damage pattern was attributed to fiber kinking in the 0° plies. The third and fourth frames ((c)–(d), (i)–(j), and (o)–(p)) indicate that, for all layups, the damage propagates on both sides of the hole before the peak load is reached. It is noted that in the Quasi laminate result shown in (j) the outer ply cracked. The fifth frame ((e), (k), and (q)) shows the frame closest to the peak load. The images shown in ((f), (l), and (r)) are taken after the load drop. Thus, the sequence of frames shows that an initial unstable damage event appears first on one side of the hole, then on the opposite side, and that this damage then propagates stably as the load increases until the specimen suddenly collapses. These observations are consistent with those reported previously [1,5]. It is remarkable that such a similar sequence of events are observed in the results for the three distinctly different layups. However, the results show only the surface behavior, which may not be sensitive to differences in the internal damage evolution. In the Hard and Quasi specimens, the shown sequence of events occurs over a short duration and small load interval near the peak load, as evident by the frame numbers and load levels of the different events. In contrast, the Soft specimens show damage relatively early, starting at 77% of peak load and the damage accumulates relatively slowly up to the peak load. These observations of surface damage are consistent with the stress vs. strain curves in that the Hard and Quasi laminates layups exhibit a relatively brittle response, whereas the response of the Soft laminate is more ductile.

The points in the load history when local bending becomes evident in the axial strain fields are shown as the open square symbols on the stress vs. strain results in Figure 2 for all of the specimens loaded to failure. Results are shown for both sides of the hole. The triangular gray symbols in Figure 2 indicate the loads where damage is visible on the interior surface of the hole in the DIC images. An example of such damage is noted by the white arrows in Figure 3b. By comparing the same locations before (frame 61 in (a)) and after the event, it is clear a change occurred. This hole surface damage is similar to that reported in [5, 6]. In the case shown, the hole surface damage occurred at the same time as the change in axial strain field, whereas in other cases the hole surface damage occurred before there was any evidence of damage in the axial strain field. The nature of the damage events noticed

(a)$f = 61, P = 89.6\%$ (b)$f = 62, P = 91.0\%$ (c)$f = 63, P = 92.6\%$

(d)$f = 66, P = 96.6\%$ (e)$f = 69, P = 100\%$ (f) Failed

(g)$f = 112, P = 94.6\%$ (h)$f = 113, P = 95.8\%$ (i)$f = 118, P = 99.1\%$

(j)$f = 119, P = 99.8\%$ (k)$f = 120, P = 100\%$ (l) Failed

(m)$f = 107, P = 77.0\%$ (n)$f = 108, P = 77.4\%$ (o)$f = 123, P = 86.9\%$

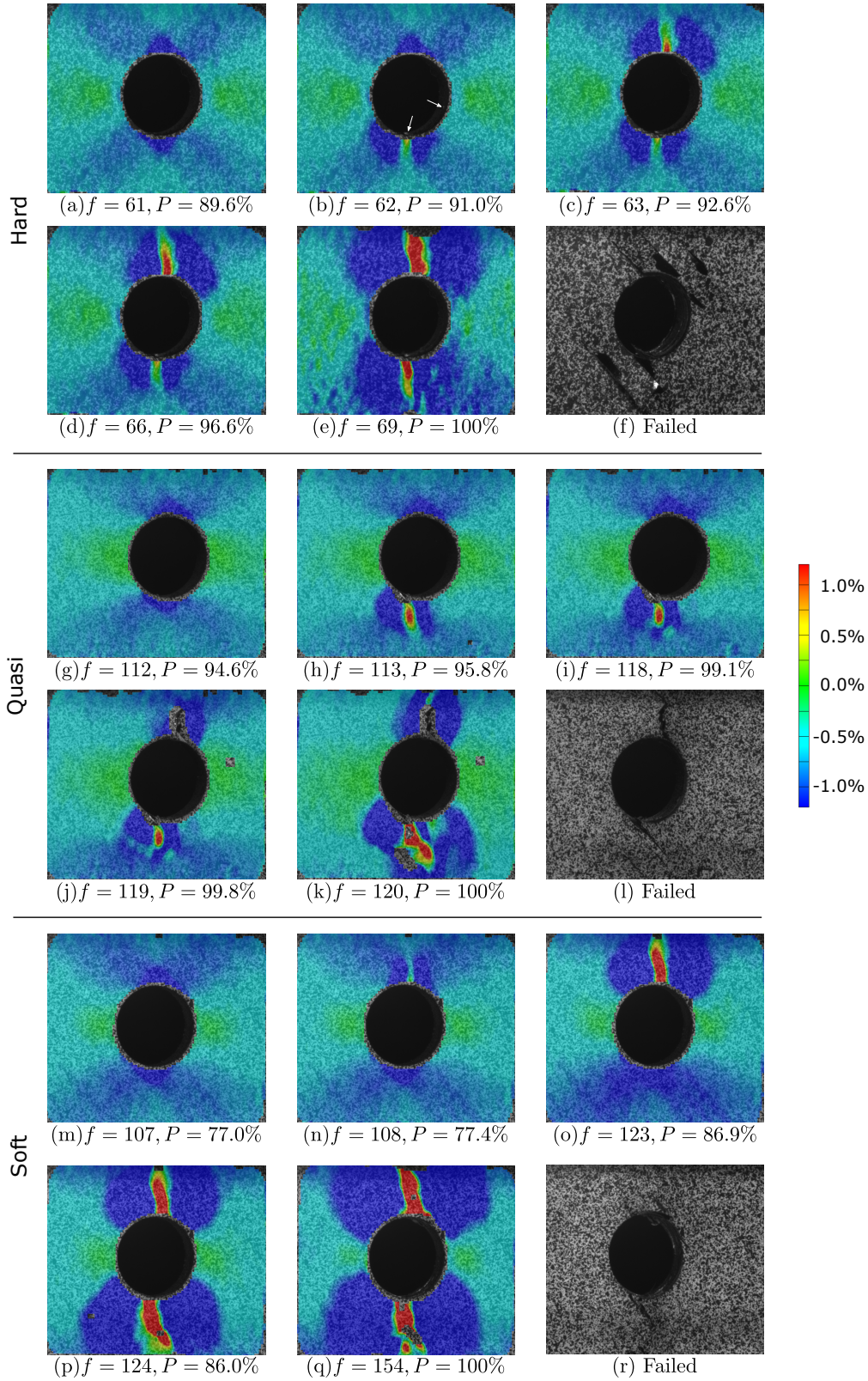(p)$f = 124, P = 86.0\%$ (q)$f = 154, P = 100\%$ (r) Failed

Figure 3: DIC results showing axial strain at several frames and the failed state for one representative specimen from each of the three layups.

on the interior surface of the holes could not be identified with the instrumentation used during these tests.

The X-Ray CT scans revealed several interesting results in terms of the damage states at the two points in the loading history where the scans were conducted. Before summarizing the observations of damage due to loading, it is noted that the scans show evidence of manufacturing-induced damage on the perimeter of the hole (i.e., from drilling) in all test specimens. The damage was determined to be from manufacturing, based on the shape and location of the damage. Examples of manufacturing-induced damage and loading-induced damage are shown in Figure 4. Two examples of cracks thought to result from drilling are marked with white arrows in Figure 4a. In general, the manufacturing damage is small and located away from the regions of maximum stress concentration, so it is assumed to be negligible for the purpose of this study. Also in Figure 4a, typical X-Ray CT imaging artifacts, seen as vertical bands slightly darker than the rest of the image, are marked with red arrows. The specimens were intentionally oriented during imaging such that most of the artifacts occur away from the main stress concentrations at the top and bottom of the hole. These artifacts (as well as other well-known X-Ray CT artifacts not shown here) occurred in all scans and are disregarded. In some scans, numerous matrix cracks were observed on one of the surface plies but not the other. These matrix cracks are considered breakout damage from drilling since it is unlikely that the nominally uniform compressive loading induced surface cracks on only one of the surface plies. Examples of loading-induced damage are shown in Figure 4b, marked by arrows. Matrix cracking is identified by the blue arrows, and a kink band is denoted by the white arrows. The damage mode is inferred by knowledge of orientation of the ply, location relative to the loading (i.e. stress state), and orientation of the damage. Though the images are all shown as planform (Figure 4c), the location and modes of damage were confirmed in the two orthogonal planes not shown. For each ply, the loading-induced damages were identified and the mode, size, and location were recorded. Only loading-induced damage is considered in the remainder of this report.

To facilitate compact visualization of the damage state through the full laminate thickness, schematic illustrations of the damage were created for each scan. The primary damage modes identified were matrix cracks and kink bands; no delaminations were identified. The results are shown in Figure 5. The left column shows data obtained at 75% average strength and the right column shows data obtained at 90% average strength. Each row corresponds to a different layup. For each scan, the hole boundary is shown with a solid black line. The damage is colored by mode as follows: red for $0°$ matrix cracks, blue for $0°$ fiber compression (kinking) damage, and teal for $-45°$ matrix cracks. Nearly all of the observed damage is in the $0°$ plies. In all scans except the Quasi laminate at the 75% level, matrix cracks are observed in all of the $0°$ plies, the longest of which among all the $0°$ plies are shown in the figure along the $0°$ direction. Hence, the figure shows the through-thickness projection of the damage state. Though only the longest matrix splitting cracks are shown, in most cases the split lengths were nearly the same in all of the $0°$ plies in each scan. One exception is the Hard 90% scan where the four-ply-thick central $0°$ ply block has very long splitting cracks on the top-right and bottom-left. Very small
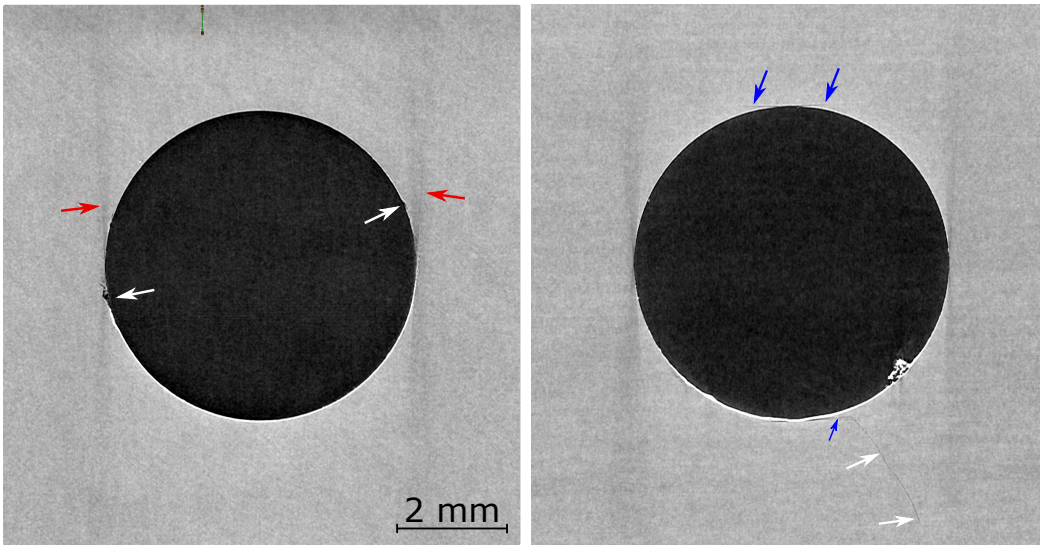
(a) Quasi, 75%, $-45°$ ply.

(b) Soft, 90%, $0°$ ply.
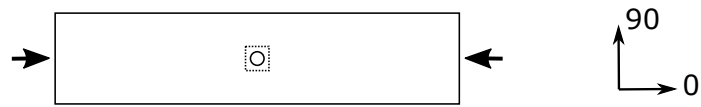
(c) Specimen schematic; the dotted rectangle showing the location of images (a) and (b).

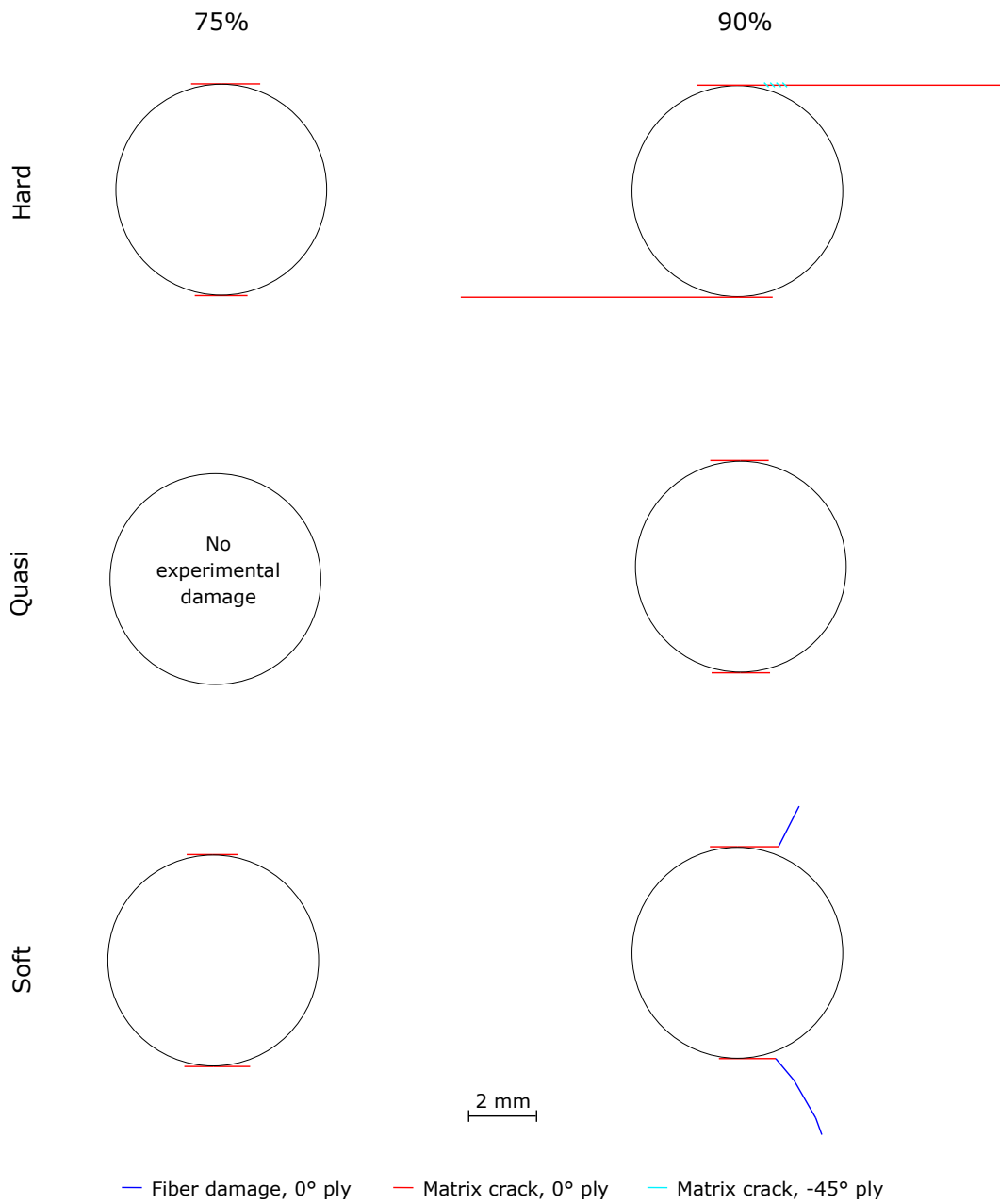Figure 4: Examples of (a) manufacturing induced and (b) loading induced damage identified in X-Ray CT data.

Figure 5: Schematics of damage from observations of X-Ray CT scans.

matrix cracks were noticed in one of the $-45°$ plies adjacent to the long splitting crack on the top right, as shown in teal in the figure. In the Soft 90% scan, fiber kinking damage was observed growing from splitting cracks. With the exception of the very small matrix cracks in the $-45°$ direction in the Hard laminate 90% scan, all of the damage occurred in the $0°$ plies, which is consistent with previously reported observations [4].

Since the 75% scan and 90% scan were taken on separate specimens, the details of the damage progression between the 75% scan and 90% scan are, at times, incompatible[1]. Thus, the experimental procedure used in this study allows for insight into the damage progression in an average sense only. A more comprehensive study wherein specimens are tested incrementally such that a time series of several X-Ray CT scans is captured through each specimen's load history would provide a concrete basis for model validation (as was done in other parts of the ACP, e.g. [23, 25, 31]).

Considering the DIC-detectable damage events on the hole surface and front surface of the specimen in the Hard and Quasi laminates, it is apparent that most of the damage occurs above the 90% peak load at which X-Ray CT data was obtained. In contrast, for the Soft laminate, the DIC data show damage onset between the 75% and 90% load levels. Since fiber kinking was observed in the Soft 90% scan, it can be inferred that the DIC-observed damage events are a result of fiber kinking in the internal $0°$ plies.

3   Model description

A parametric PDFA model of the standard OHC specimen for use with Comp-Dam was developed previously [22] using the Abaqus Python interface [32] and is extended herein. The Python interface is used to generate the models with a fiber-aligned ply-by-ply meshing strategy. The specimen dimensions, locally refined region dimensions, layup, and several other characteristics of the model are defined parametrically in the scipt for ease of use. The nominal model geometry, boundary conditions, discretization, and material properties of the model used are described in this section.

The model geometry and boundary conditions are shown in Figure 6a. The model width and hole diameter are the nominal test specimen dimensions. The model length is reduced since it is not necessary to model the full gripping region. The local region near the hole, shown as the 20 mm wide gray band in Figure 6a, is allowed to damage, whereas the remaining transition region (blue in Figure 6a) and far-field regions of the specimen (white in Figure 6a) are modeled as linear elastic. Uniaxial loading is applied via prescribed end shortening. Out-of-plane displacements were set to zero in the transition and far-field regions to mimic the OHC test fixture.

The model was meshed with a combination of solid continuum, continuum shell, and cohesive elements. A planform view of a typical mesh is shown in Figure 6b

---

[1]Specifically, in the Hard laminate, some of the split lengths in the 2-ply-thick $0°$ ply blocks are longer in the 75% scan than in the 90% scan. This is not visible in Figure 5 since the figure shows the maximum extent of each damage mode.
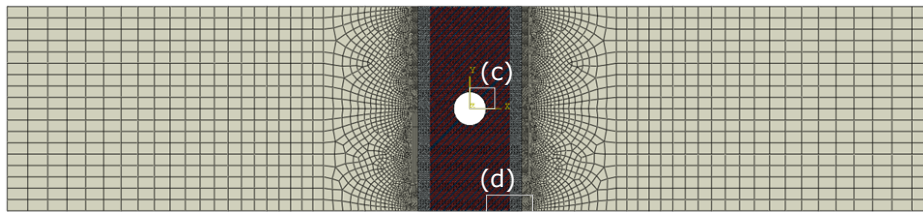
with accompanying detail views of the hole boundary in Figure 6c and the mesh transition region in Figure 6d. The model was constructed to create a smooth transition between the coarse far-field and highly refined near-field in order to minimize spurious stress concentrations at the boundary of the local region. The far-field region is composed of one layer of continuum shell elements (SC8R) through the thickness with the in-plane mesh size transitioned to the target local mesh size near the transition region. The local and transition regions are discretized with one layer of fiber-aligned reduced-integration continuum elements (C3D8R) for each ply. The elements in Figure 6b–6d are colored by the section definition as follows. The beige elements are in the far-field region and have a composite shell section definition with linear elastic material response. The gray elements in the transition region have a solid section definition with linear elastic material response. Tie constraints were used to connect the transition region (1 element per ply thickness) to the far-field region (1 element per laminate thickness). The blue elements in the local region have both fiber and matrix damage enabled. The red elements allow fiber damage but do not allow matrix cracking such that a minimum crack spacing is introduced. The minimum crack spacing is kept constant through this work, with every 4th row of elements being allowed to have a matrix crack (see [22]). The meshing and section assignments were implemented such that matrix cracks could occur tangent to the hole in all plies, as shown in Figure 6c for a 0° ply. In the local region, when two adjacent plies have the same direction, they share nodes at the ply interfaces. For dissimilar ply interfaces, the layers are connected using node-based tie constraints to a layer of zero-thickness cohesive elements (COH3D8) to model delamination. In Figure 6d, the elements in a triangular region of the 45° ply are hidden, revealing the adjacent layer of cohesive elements, which are shown in green. The cohesive layer meshes are always aligned with the loading direction and they have the same planform size as the corresponding continuum elements. Wedge elements are used near the free edges of the local region to preserve the fiber-aligned mesh and at the same time have smooth boundaries. Since relatively few wedge elements are used, and no verification of the damage modeling procedures used herein have been completed so far for wedge elements, they are modeled as linear elastic, and hence colored in gray. In-plane mesh sizes of 0.15, 0.2, and 0.25 mm were considered to evaluate the element size sensitivity of the results. These element sizes were chosen based on results from previous verification studies [18, 19] that suggest 0.2 mm is about the maximum allowable element size. Except where noted otherwise, the results shown are for the 0.2 mm mesh size.

CompDam is used as the material model for all of the continuum elements. The plies are assumed to be transversely isotropic. Delamination in the cohesive interface elements was modeled using the built-in Abaqus material model with a bilinear traction separation law.

The nominal material properties are listed in Table 3. The material properties are taken from reference [17], which has been used throughout the related ACP activities. These material properties were obtained from published data [33] and from tests sponsored by the ACP. Although the OHC analyses were conducted after the testing with full view of the test results, the nominal material properties were established prior to the OHC test and they remained unchanged throughout the
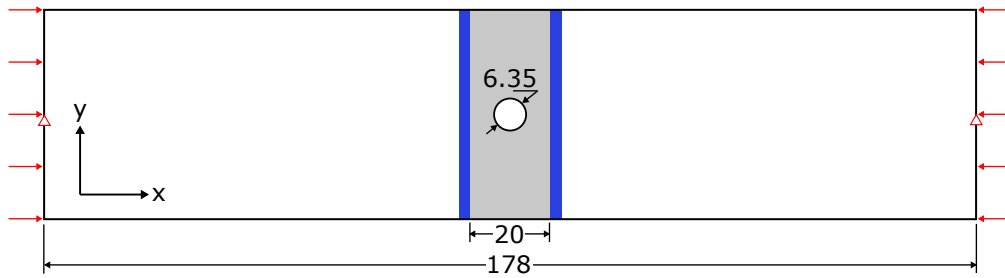
(a) Geometry and boundary conditions (units are mm).

(b) Mesh, colored by section.
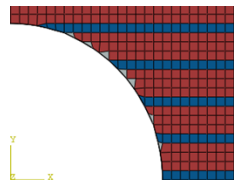
(c) Mesh, 0° ply near hole.

(d) Mesh, 45° ply, transition.

Damageable

■ Fiber damage enabled

■ Matrix cracking and fiber damage enabled

■ Cohesive interface elements

Not damageable

□ Transition

□ Far field

Figure 6: Finite element model overview.
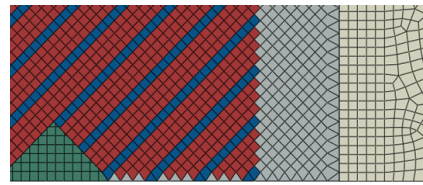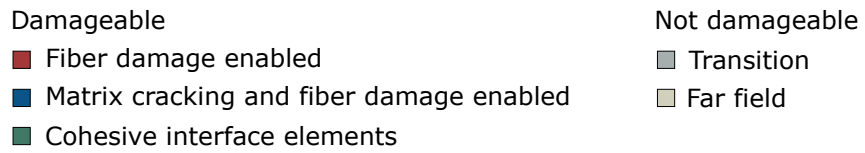
Table 3: Nominal material properties [17].

	Symbol	Value	Units
	E_{11}	140653	MPa
	E_{22}	8703	MPa
	G_{12}	5164	MPa
Elastic	ν_{12}	0.32	-
	ν_{23}	0.45	-
	α_{11}	-5.5×10^{-6}	$/^{\circ}C$
	α_{22}	2.58×10^{-5}	$/^{\circ}C$
	Y_T	80.1	MPa
	Y_C	288.2	MPa
	S_L	97.6	MPa
Matrix damage	G_{Ic}	0.24	kJ/m^2
	G_{IIc}	0.739	kJ/m^2
	η_{BK}	2.07	-
	X_C	1731	MPa
	G_{FC}	61	kJ/m^2
Fiber damage	m	0.5	-
	n	0.2	-

project[2].

Matrix cracking is modeled using the deformation gradient decomposition (DGD) technique [28]. The matrix crack surface is defined by a normal having an angle α with respect to the transverse direction of the ply. Herein, $\alpha = 0$ was set as an initial condition because of occasional convergence difficulties in the DGD algorithm. Limited spot checks showed that the structural response and damage were similar with and without the $\alpha = 0$ restriction.

CompDam has multiple models available for fiber compression. In this work, the conventional CDM model is used with a trilinear stress-strain law. The softening law is defined by the strength X_C, toughness G_{FC}, and two parameters m, n that specify the knee in the curve. When $m = n = 0.5$ the shape of the softening portion of the law is linear. For the case herein where $n = 0.2$, the softening portion is concave. The fiber-direction stress-strain law is plotted assuming the element size is 0.2 mm in Figure 7. The solid black line represents the nominal stress-strain law for fiber compression used in the analyses. Since the values of m, n used in the present analyses (Table 3) were established prior to the availability of material property characterization data, the selected values are discussed in the context of relevant characterization data (gray lines in Figure 7) in the remainder of this paragraph. The two gray lines are derived from R-curves measured using the size-effect law approach proposed by Catalanotti et al. [34] wherein a series of double-edge-notched-compression (DENC) specimens are tested and the R-curve is

---

[2]The coefficients of thermal expansion, α_{11} and α_{22}, were only used in analyses that were evaluated to examine the effect of a thermal cool down step for consideration of the role of thermal residual stresses, as described in Section 6.1.
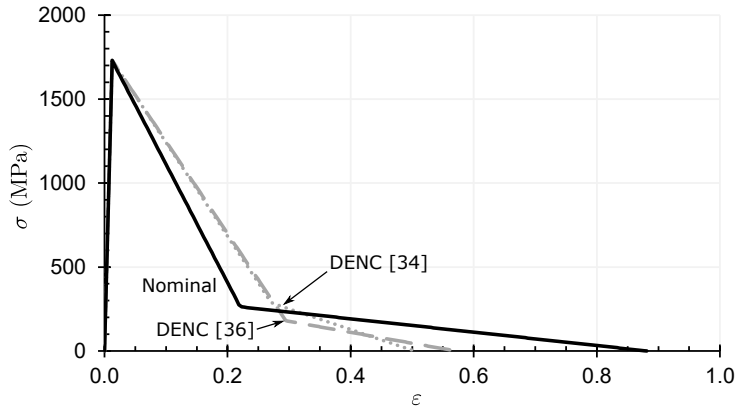
Figure 7: The nominal fiber direction stress-strain law assumed in the model and stress-strain laws obtained from R-curves measured for IM7-8552 using the size effect law.

back-calculated from the measured size effect. The gray trilinear stress-strain laws are obtained from the R-curves using the procedure described in [35]. The dotted line is based on the R-curve from [34] for a specification of IM7/8552 similar to the one used herein and corresponds to $m = 0.35$ and $n = 0.5$. The dashed line is based on the R-curve measured using DENC specimens fabricated from the same materials and using the same processing as for the present OHC specimens, reported in [36], and corresponds to $m = 0.34$ and $n = 0.21$. It can be observed that the three stress-strain laws are similar. Hence, errors resulting from the assumed trilinear law (black) compared with the measured trilinear laws (gray) are assumed to be small[3]. The four properties that define the fiber compression direction softening law (X_C, G_{FC}, m, and n) are all challenging to measure and the results are expected to be sensitive to the values used since they control fiber damage onset and propagation. Thus, the sensitivities of the predictions to these properties are investigated in Sections 6.2 and 6.3.

Quasi-static loading was modeled using Abaqus/Explicit. The prescribed displacement was applied with a smooth step amplitude through a 0.2 second dynamic step. Mass scaling was introduced with the automatic mass scaling option such that typical analyses used 1.5 million increments to reach peak load and the element mass in the local region was scaled by about 10^3 for the 0.2 mm element size. Detailed investigation showed that this was sufficient to almost completely suppress dynamic effects until after the peak load is reached (see Section 5).

4 Results using the nominal parameters

The predictions from the model as described above (referred to as the nominal configuration) are reported and discussed in this section. First, the overall specimen

---

[3]This assumption was verified for the Soft laminate, 0.2 mm element size.

response is presented. Then, the evolution of damage is described. Comparisons are made with the experimental results where possible.

4.1   Stress vs. strain response

The measured and predicted specimen stress versus strain responses are shown in Figure 8. The test results are shown as solid lines (repeated from Figure 2) and the analysis results are shown as dashed lines. Analysis results for three mesh sizes are shown in the figure and labeled as such (0.15, 0.2, and 0.25) with the results obtained using the smallest element size having the darkest lines with the shortest dashes. The results from analyses are plotted up to the point where the analyses terminated, which is after the peak load is reached and the load decreases. The analyses terminated due to numerical errors from excessive distortion of damaged elements. Element deletion would provide a means to continue the analyses further, but rapid increase of kinetic energy after peak load combined with the use of mass scaling diminish the physical relevance of the post-peak results. The initial stiffness, strength, and strain-to-failure are listed for each laminate along with percent errors in Table 4. The percent errors are calculated using the experimentally measured values reported in Table 2 as the reference values. Good overall agreement is noted for all cases in terms of initial stiffness. The Hard laminate stiffness is under-predicted by about 8%, whereas the stiffness for the other laminates agree within 2%. One reason for this difference could be that the E_{11} value used is slightly low, and that the zero-dominated Hard layup is most sensitive to this property. The Soft laminate tests show a slightly nonlinear response from about 0.55% strain to the first load drop around 0.75% strain, which was not captured by the analysis. Since the Soft laminate is mostly 45° plies, the slight nonlinearity in the response could be due to shear nonlinearity characteristic in ±45° laminates (see, e.g., [37]).

The predicted strengths and corresponding strain-to-failure are in relatively good agreement for the Hard and Quasi laminates, especially for the 0.15 mm mesh size for which the errors are less than 5%. In contrast, the predicted failure for the Soft laminate occurs near the first load drop in the test data. The Soft laminate test data shows a series of small load drops and a reduced effective stiffness up to the peak load, which occurs at around 1.15% strain. The predicted failure for the Soft laminate occurs early at around 0.77% strain, so the strain-to-failure is in relatively poor agreement with the experimental values, with about 30% error.
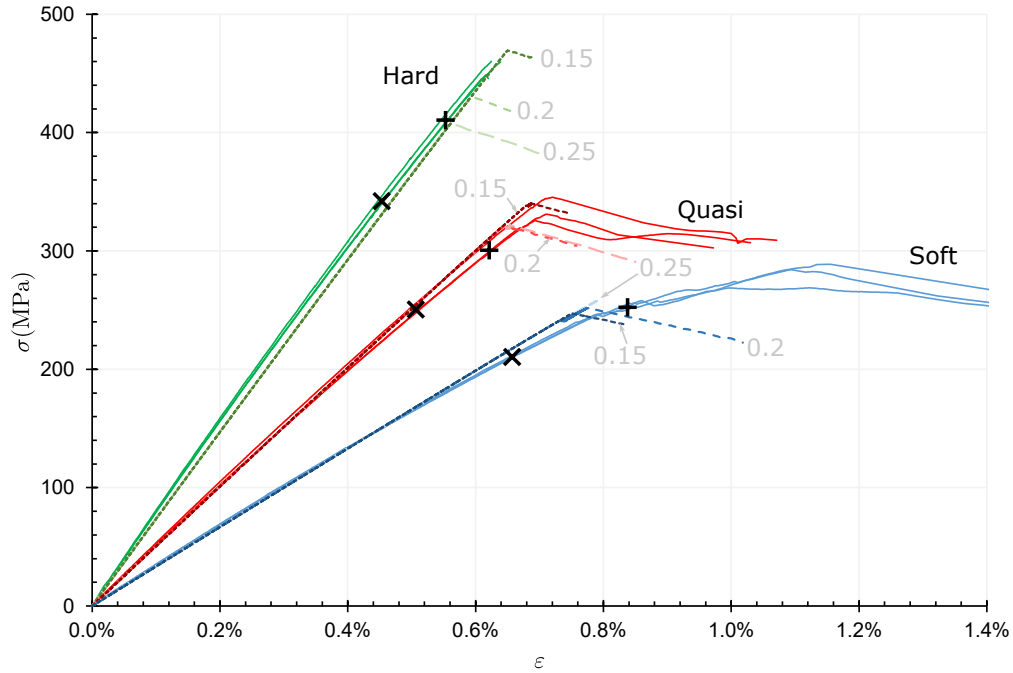
Figure 8: Comparison of test (solid lines) and analysis (broken lines) nominal stress vs. strain response. The 'x' and '+' markers denote X-Ray CT scans.

Table 4: Predicted stiffnesses, strengths, and strain-to-failures with percent errors calculated using the corresponding experimental averages.

Layup	Mesh size (mm)	Stiffness E_{pda} [GPa]	% error	Strength $\sigma_{\mathrm{c,pda}}$ [MPa]	% error	Strain-to-failure $\varepsilon_{\mathrm{c,pda}}$ [%]	% error
	0.25	73.62	-7.65	407.3	-10.7	0.561	-10.3
Hard	0.20	73.61	-7.66	429.7	-5.8	0.594	-5.1
	0.15	73.60	-7.68	469.2	2.8	0.654	4.5
	0.25	50.53	-1.72	321.4	-3.8	0.654	-7.7
Quasi	0.20	50.52	-1.72	320.8	-3.9	0.644	-9.0
	0.15	50.51	-1.74	340.2	1.8	0.686	-3.1
	0.25	33.34	-1.60	257.6	-8.2	0.789	-29.8
Soft	0.20	33.34	-1.60	251.8	-10.3	0.774	-31.1
	0.15	33.33	-1.62	247.2	-11.9	0.751	-33.1

4.2 Damage evolution

The predicted nominal stress vs. strain responses are a direct consequence of the predicted damage evolution and resulting stress redistributions in the plies. Therefore, to gather more insight into the predicted response, the damage evolution is examined in detail in this section. In general, OHC specimens are expected to collapse due to one of two failure mechanisms: delamination leading to sublaminate buckling or fiber compression damage. While both mechanisms may occur, the results are evaluated to determine which mechanism is responsible for the loss in load carrying capability. The sequence of damage events as predicted by the analysis is presented and discussed for each layup. A series of damage states were extracted from the analysis results for each of the three layups to illustrate the predicted damage evolution leading to structural collapse. The results are presented in the same format for each layup with the 0.2 mm mesh. The results are interrogated to determine the failure mechanism. This discussion focuses exclusively on the results from the analysis, since the test observations were insufficient to characterize the damage evolution during the rapid succession of events near the peak load.

4.2.1 Damage evolution in the Hard laminate

The damage states for the Hard layup are shown in Figure 9. In this figure (and Figure 14 and Figure 17 for Quasi and Soft, respectively), a grid is used to display the 4-D data (3-D and time/load). Each column corresponds to a specific nominal stress level, labeled along the top as a percentage of the predicted strength ($\sigma_{\mathrm{pda}}/\sigma_{\mathrm{c,pda}}$). After the peak load is reached, the post-peak loads are denoted with PP. Each row corresponds to a subset of the plies and ply interfaces, labeled along the left of the figure where the numeric orientation indicates the ply and the '/' indicates the ply interface. The damage is colored to distinguish the ply or ply interface in which the damage occurs with the colors used shown next to the labels on the left of the figure. Since the damage was relatively symmetric, half of the laminate is described. The ply group at the outer surface is shown in the first row and the ply group at the midplane is shown in the last row. By showing only a few plies in each image (i.e. a "ply group"), the damage at each ply and ply interface can be distinguished. The region shown is selected such that the damage in the post-peak state fits within the region (i.e., the damage is not truncated). In each image, the damage state shows matrix cracks and compressive fiber damage in the plies and delamination at ply interfaces. In the cases where the 0° plies have matrix cracks and fiber damage, the damage modes are distinguished with a checkerboard pattern[4]. The damage state is obtained by showing only elements with matrix damage variables $d2 \geq 0.9999$ (equivalent to 99.6% fracture toughness dissipated) or fiber damage variables $d1c \geq 0.9$ (equivalent to 21.8% fracture toughness dissipated, or equivalently 8.7% strain in Figure 7) in their undeformed state. The threshold for fiber damage is a low value to facilitate visualization since $d1c$ never reaches a large value where nearly all of the energy has been dissipated (e.g., as used for matrix cracks and delaminations). The particular

---

[4]On the pdf version zoom in to see the checkerboard; it may appear black when zoomed out or printed.

load levels were selected as follows: the first three load levels are the closest output frame to 75%, 90%, and 97% of the predicted peak load; the fourth load level is at the peak load; and the fifth and sixth load levels are after the peak load showing the damage progression associated with the unloading.

The pre-peak damage states in the results for the Hard layup shown in Figure 9 include mostly matrix cracks with very little delamination. Most matrix cracks initiate and propagate tangent to the hole in the 0° and 45° plies. Generally, the cracks extend longer in the two-ply-thick and four-ply-thick ply blocks as well as the surface plies as compared with the single plies, which is expected based on the in-situ effect (see, e.g., [38]). In addition to the cracks tangent to the hole, matrix cracks occur in the center (width-wise, $\beta = 0°$ and $180°$) of the specimens in some plies due to the local tensile stress concentration at this location. As the laminate's strength is reached, fiber damage grows rapidly in the 0° plies and large delaminations occur at the 45/0 interfaces. The results shown are for the 0.2 mm mesh size. The damage sequence for the Hard layup predicted using the 0.15 mm mesh was similar. The results using the 0.25 mm mesh differed substantially in that no long splitting cracks in the central four-ply-thick 0° were predicted, which is thought to be a result of mesh size sensitivity in long-crack propagation that is known to become significant around 0.25 mm mesh size for this material system [18].

It is unclear from the results presented in Figure 9 if the predicted collapse occurs due to fiber damage, delamination (i.e. sub-laminate buckling), or a combination of the two mechanisms. Compressive fiber damage and delamination area are overlaid on the stress-strain curve in Figure 10 to help clarify the predicted failure mechanism. In the figure, the stress-strain curve is the thick black line plotted using the left ordinate. Data are provided for normalized stress levels ranging from 0.99 to 1.0. The maximum fiber damage variable ($d1c$) value in each 0° ply block is plotted as solid colored lines using the right-most ordinate. Results for the four-ply-thick ply block are shown in red and results for the two-ply-thick ply blocks are shown in blue, with the results from the outermost ply blocks shown in light blue. The results from the two-ply-thick 0° plies symmetric about the laminate mid-plane are nearly identical. The dashed lines are the cumulative delaminated area for each ply interface. The delaminated area is approximated by the number of elements with $d2 \geq 0.9999$ times the nominal element edge length squared. Since some elements near the hole have a smaller than nominal area, this approximation slightly overestimates the delamination area. Nonetheless, the trends in delamination area growth are captured. Only half of the ply interfaces are shown for clarity, since, like the fiber damage results, the delaminated area was relatively symmetric about the mid-plane of the specimen. The delaminated area curves cluster into groups at strains above about 0.62%. The curves are colored by group to highlight this pattern where the gray lines are +45/−45 interfaces, the blue lines are $\pm45/0_2$ interfaces and the red line is the $-45/0_4$ interface. Dotted vertical gray lines are overlaid at two key strain levels: 0.5970% where a change in stiffness occurs just before peak load and 0.5985% where the stress starts decreasing rapidly just after peak load. The data in the plot were extracted from field outputs, with a higher frequency of output starting just
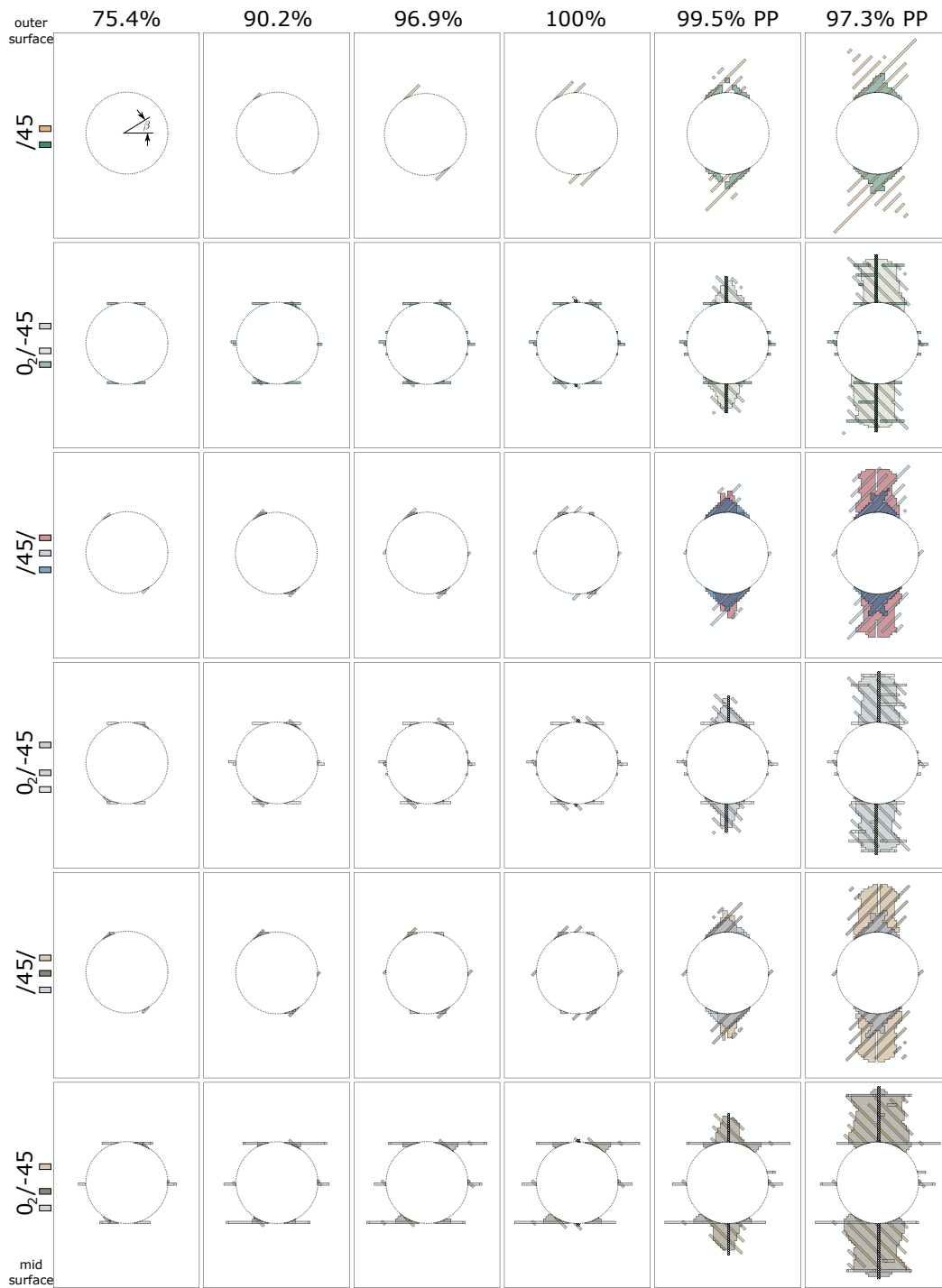
Figure 9: Analysis predicted damage states at several load levels for the Hard layup. The load of each image is shown across the top as $\sigma_{\mathrm{pda}}/\sigma_{\mathrm{c,pda}}$ (PP indicates post-peak), and the ply group is labeled along the left.
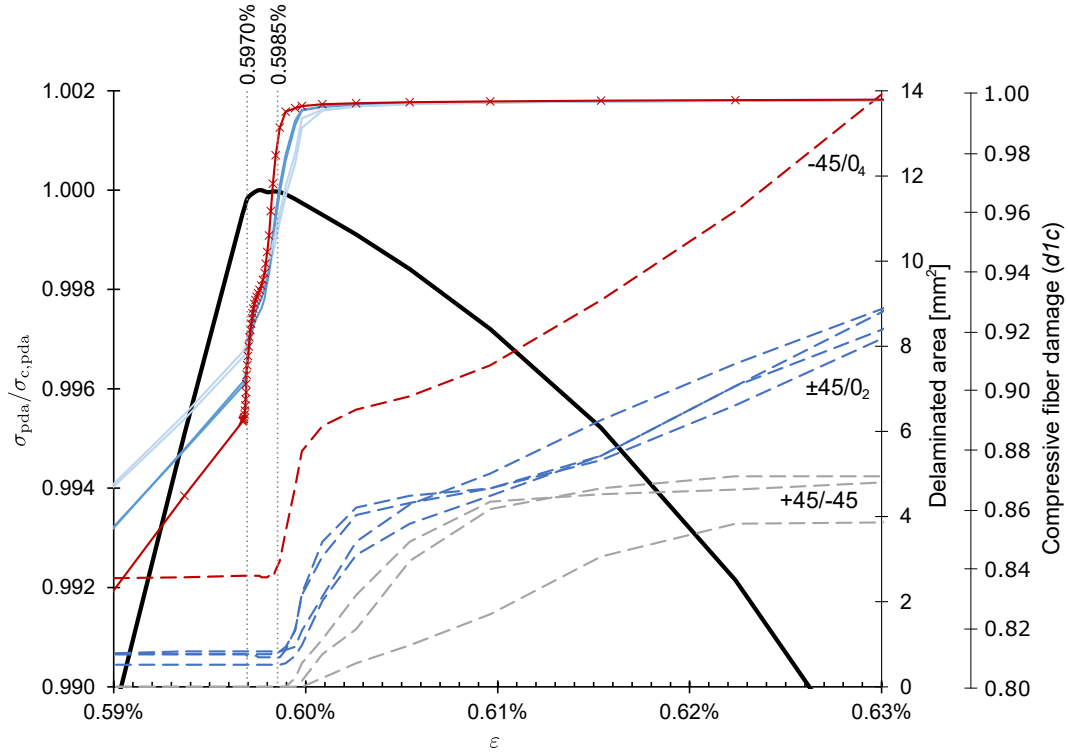
Figure 10: Normalized stress (solid black line), fiber damage (solid colored lines), and delaminated area (dashed lines) vs. nominal strain for the Hard laminate.

before 0.597% strain[5].

The results show fiber damage ($d1c$) increasing above about 0.9 between about 0.597% and 0.5985% strain coincides with the peak of the stress-strain response. During the same range of strains, the delaminated area is constant. Therefore, it is evident that the model predicts that the final failure sequence initiates as a result of fiber damage. The fiber damage increases fastest in the four-ply-block, suggesting that this is the most critical 0° ply block. At 0.5985% strain, the delaminated area starts increasing rapidly, and shortly after the fiber damage plateaus, reaching a maximum value of 0.997 (equivalent to 72% fracture toughness dissipated, or equivalently 47% strain in Figure 7). The increase in delaminated area coincides with the load drop. In addition, when the delamination area grows, there is an abrupt increase in out-of-plane deformation in the surface plies in the same region as the delamination. Considering these results together, the predicted failure sequence is: 1) triggered by fiber damage, which results in 2) delamination at the interfaces adjacent to the 0° ply blocks, and then 3) sub-laminate buckling. It is noted that

---

[5]The frequency of the outputs changes at around 0.597% strain, as shown by the markers (x) on the red curve ($d1c$ for the four-ply-thick 0° ply block). Markers are shown only on one curve for clarity, though the data are extracted at the same analysis time points for all the curves. Attention is brought to this detail since, if more output frames were requested, a smooth change in slope of the d1c curves would be seen at around 0.597% strain.
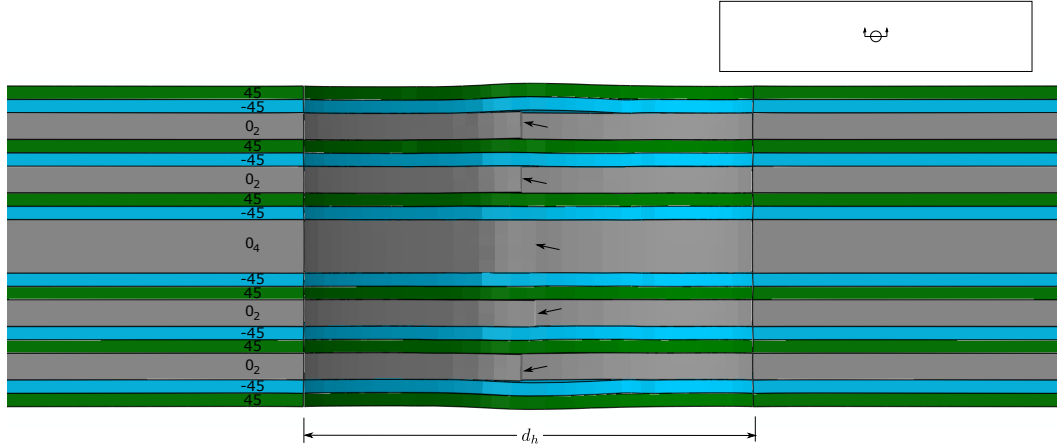
Figure 11: Deformed cross section of the Hard laminate at 97% post-peak load level predicted by the 0.2 mm mesh model. The arrows point to localized fiber damage.

with one C3D8R element through the thickness of each ply, the bending stiffness of the delaminated plies is inaccurate. Therefore, the sub-laminate buckling response should be examined further.

A cross section view showing the deformed state of the plies at the 97% post-peak load level is shown in Figure 11. The elements where fiber damage has localized are marked with an arrow. In the two-ply blocks, the fiber damaged elements shear out-of-plane and open delaminations develop adjacent to the fiber damage. The central four-ply-block appears to crush without any significant out-of-plane deformations.

In the central four-ply-thick 0° ply block, matrix splitting cracks initiate below 75% peak load and propagate several millimeters by peak load. The behavior of these splitting cracks is investigated in more detail since they contribute to the final failure sequence by blunting the compressive stress concentration that eventually triggers failure as described above. The lengths of these cracks as a function of the nominal strain are plotted in Figure 12. The four splitting cracks are labeled in the schematic in Figure 12a and shown in pairs. The lengths of splits B and C are shown in Figure 12b and the lengths of splits A and D are shown in Figure 12c. Observations from the X-Ray CT data show that the cracks B and C grew to longer lengths than the cracks A and D (see Hard laminate, 90% in Figure 5). It is noted that the same trend was observed experimentally for the same layup in [2]. Measurements of the split length are shown in the figure as open circles for the 75% scan (0.46% strain) and the 90% scan (0.56% strain). The analysis results are shown as green, orange, and blue lines for the 0.15, 0.2, and 0.25 mm mesh sizes, respectively. The analysis results are shown for one of the two splits in each pair (i.e. B is shown in Figure 12b and A is shown in Figure 12c) since the corresponding split in the pair had virtually identical behavior. Considering the analysis results from the 0.2 mm mesh, the experimental trend of anti-symmetric split lengths is reproduced by the analysis. Between 0.5% and 0.55% strain, splits B and C grow rapidly to about 3.5 mm. At higher strains, the splits continue to grow to greater
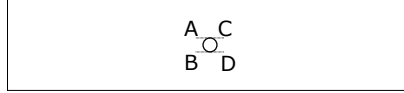
(a) Schematic showing four matrix splitting crack locations as A, B, C, and D.
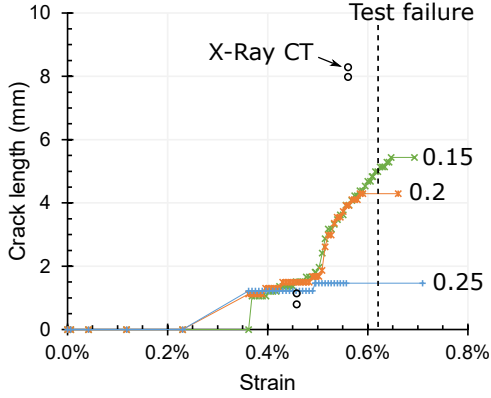
(b) Locations B and C.
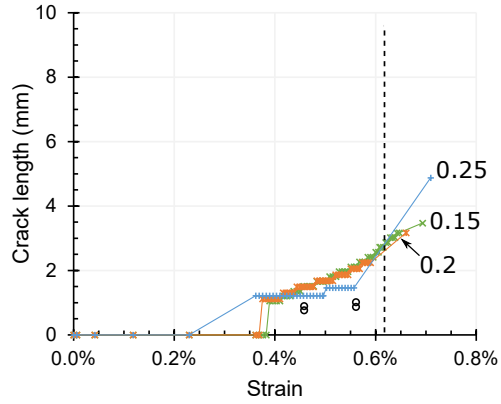
(c) Locations A and D.

Figure 12: Lengths of splitting cracks in the central ply block of the Hard layup.

than 4 mm, but at a slower rate, until the peak load is reached. In contrast, the splits A and D grow steadily to about 3.2 mm when peak load is reached. The analysis results for the 0.15 mm mesh show the same behavior, with one difference being that the splitting cracks at B and C are about one millimeter longer at peak load. The results for the 0.25 mm mesh show a different response. The splitting cracks remain between 1 and 2 mm at all four locations until the peak load is reached. It is concluded that the 0.25 mm mesh size is too coarse to properly represent these matrix splitting cracks. In [18], the 0.25 mm mesh size was found to be acceptable based on the studies conducted for matrix crack propagation using a similar set of material properties. The more limiting mesh size requirement identified here could be a result of matrix crack and delamination interaction, which was not considered in [18]. Quantitatively, the analysis results largely undershoot the 8 mm split lengths measured in the 90% scan at locations B and C. This difference might be due to ignoring residual thermal stresses in the analysis, as discussed in Section 6.1.

The anti-symmetry in the matrix splitting crack lengths shown in the test data in Figure 12 and Figure 5 is a result of the neighboring ply orientation. The model explains the mechanism qualitatively as shown in Figure 13 for the 0.15 mm mesh. The first row of images, Figure 13a–13c, are extracted just after the point of damage onset in the region highlighted in gray in the schematic at the bottom left of the figure. The second row of images, Figure 13d–13f, are extracted after significant propagation has occurred, just before peak load. In Figure 13a, the matrix cracks are shown via the matrix damage variable, $d2$, contour plot for the central $0°$ ply block. The splitting cracks noted previously are observed and annotated A–D. At this point in the loading history, the lengths of the splitting cracks are approximately

26

(a) Central 0°, d2.　　　　(b) Adjacent −45°, d2.　　　　(c) Adjacent −45°, FIm.

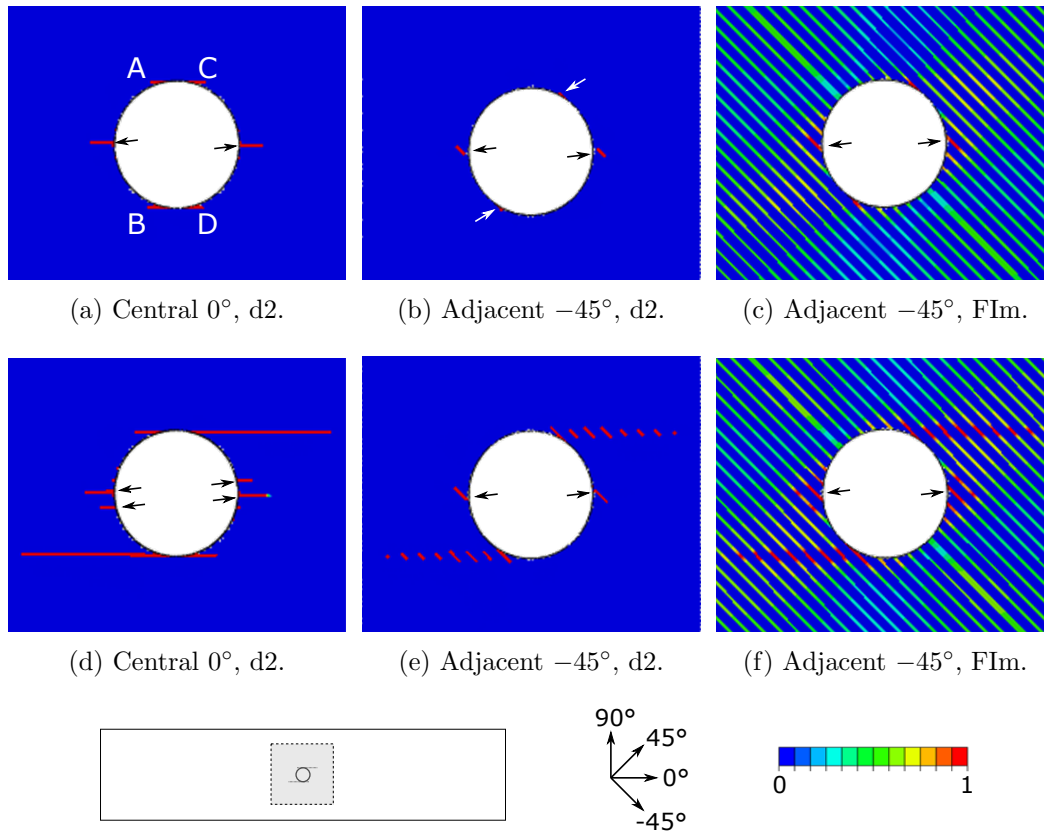(d) Central 0°, d2.　　　　(e) Adjacent −45°, d2.　　　　(f) Adjacent −45°, FIm.

Figure 13: Interaction between matrix splitting cracks in the central 0° ply and adjacent −45° plies. (a)–(c) show the state just after the initiation of the splitting cracks and (d)–(f) show the state after significant propagation has occurred (before peak load).

equal. The matrix damage variable contour plot is shown for an adjacent $-45°$ ply in Figure 13b wherein minute matrix cracks are noticed at locations B and C and annotated with white arrows. No matrix cracks have occurred at locations A and D. The matrix crack failure index is shown in Figure 13c to highlight the difference in the stress state at locations B and C vs. A and D. At locations A and D the failure index is about 0.5, with damage onset occurring when the failure index reaches 1.0. Thus the local stress state at locations A and D in the neighboring $-45°$ plies does not promote matrix cracking. The corresponding results for a later frame in the analysis are shown in Figure 13d–13f highlighting that while numerous cracks develop in the adjacent $-45°$ ply along the splitting cracks B and C, no matrix cracks occur near locations A and D due to the local stress state resulting from the combination of the ply orientation and the sign of the shear stress. Since the adjacent $-45°$ plies do not crack at locations A and D, these $-45°$ plies share the shear stress with the $0°$ ply, therefore reducing the driving force for splitting crack growth. In contrast, at locations B and C, the shear stress is along the adjacent ply direction. As a result, the $-45°$ plies crack causing more of the shear stress to be carried by the $0°$ ply thereby increasing the driving force to grow the splitting cracks. In summary, interaction between matrix cracking in the two plies explains the anti-symmetric split lengths in the central $0°$ ply block. Referring back to Figure 5 for the Hard layup at 90% peak load, a pattern of several short matrix cracks in the $-45°$ ply adjacent to the central $0°$ was identified in the test results (shown with teal lines in the figure). This damage pattern resembles the damage predicted in Figure 13e. The correlation between the observed and predicted damage patterns supports the validity of the model in terms of its ability to capture the interaction between matrix cracking in these two plies.

In Figure 13, additional matrix cracks are shown that warrant some discussion. The black arrows point to matrix cracks that are predicted to occur due to local tension from Poisson's effect. These cracks are discussed in more detail in Section 4.3.

4.2.2 Damage evolution in the Quasi laminate

The damage states predicted for the Quasi layup are shown in Figure 14, using the same format described above for Figure 9. The pre-peak damage states include short matrix cracks with very little delamination. Most matrix cracks initiate and propagate tangent from the hole in the $0°$ and $45°$ plies. At the peak load, some fiber damage is noticed in the inner $0°$ plies. Small delaminations are seen at the corresponding 45/0 interfaces. After the laminate's strength is reached, fiber damage grows rapidly in the $0°$ plies and large delaminations occur at several interfaces, with the largest delaminations being in the 45/0 interfaces. The delamination regions are bounded and connected by matrix cracks. The results shown are for the 0.2 mm mesh size. The damage sequence for the Quasi layup predicted using the 0.15 mm and 0.25 mesh was similar to that of the 0.2 mm mesh. In general, the smaller mesh sizes produced longer matrix cracks and larger delaminations at the same load level.

The details of the failure sequence near the peak load are shown in Figure 15, following the same pattern as Figure 10. The stress-strain curve is the thick black line plotted using the left ordinate, showing just 1% of the response at the strength.

The history of the maximum fiber damage variable ($d1c$) value in each $0°$ ply block in half the laminate is plotted in the colored lines using the right-most ordinate. From the $0°$ ply nearest to the outer surface to the $0°$ ply nearest to the specimen midplane, the results are shown with solid orange, blue, and green lines, respectively. The dashed lines are the cumulative delaminated area for each ply interface. Only half of the ply interfaces are shown for clarity, since, like the fiber damage results, the delaminated area was relatively symmetric about the mid-thickness plane of the specimen. The delaminated area curves are colored corresponding to the adjacent $0°$ ply if next to $0°$; otherwise they are shown in gray. The results show an increase in both fiber damage and delaminated area starting at 0.65% strain, which coincides with nonlinearity in the stress-strain curve. At slightly higher strain, when the strength is exceeded, both fiber damage and delaminated area increase rapidly. Therefore, both mechanisms acting together appear to be responsible for the loss of load carrying capability. At the strain levels around the peak load, the $0°$ ply with the most damage (the innermost $0°$, orange), has the largest delaminations at the adjacent interfaces. Likewise, the $0°$ ply with the least damage (the outermost $0°$, green), has the smallest delaminations at the adjacent interfaces. After the peak load, at around 0.657% strain, this trend ends and the largest delaminated area is in the 0/-45 interface. As was observed for the Hard laminate, the fiber damage plateaus, reaching a maximum value of 0.997 (equivalent to 72% fracture toughness dissipated). Although the delaminated area and fiber damage begin to rapidly increase at the same time, it can be inferred that the primary collapse mechanism is fiber damage since the delaminated area at the peak load and shortly after is very small (< 2 mm^2), and therefore sub-laminate buckling does not occur until after the load has decreased substantially.

A cross section view showing the deformed state of the plies at the 97% post-peak load level is shown in Figure 16. The elements where fiber damage has localized are indicated with an arrow for each $0°$ ply. It is noted that the fiber damaged elements shear out-of-plane and large open delaminations develop adjacent to the fiber damage.

(a) Ply groups 1–6.
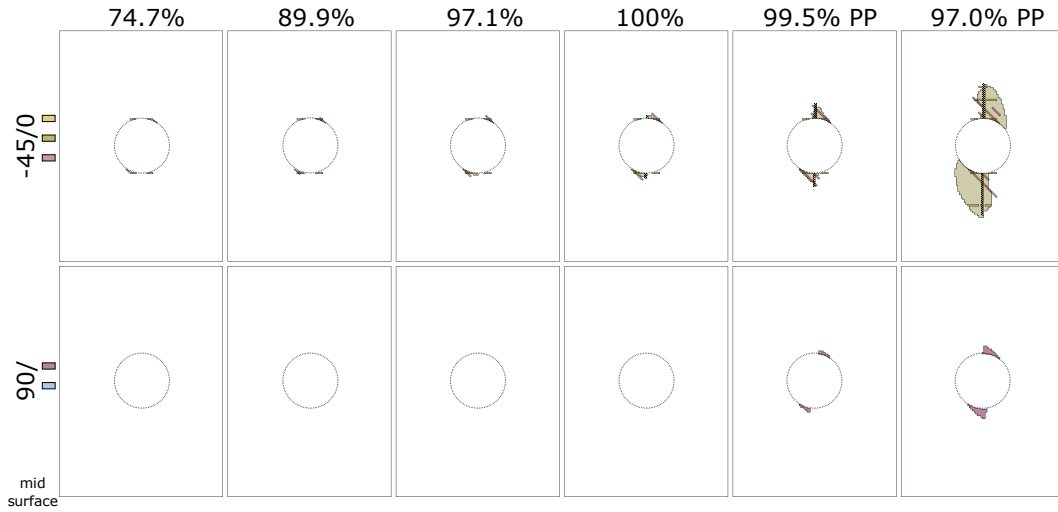
(b) Ply groups 7 and 8.

Figure 14: Analysis predicted damage states at several load levels for the Quasi layup. The load of each image is shown across the top as $\sigma_{\mathrm{pda}}/\sigma_{\mathrm{c,pda}}$ (PP indicates post-peak), and the ply group is labeled along the left.
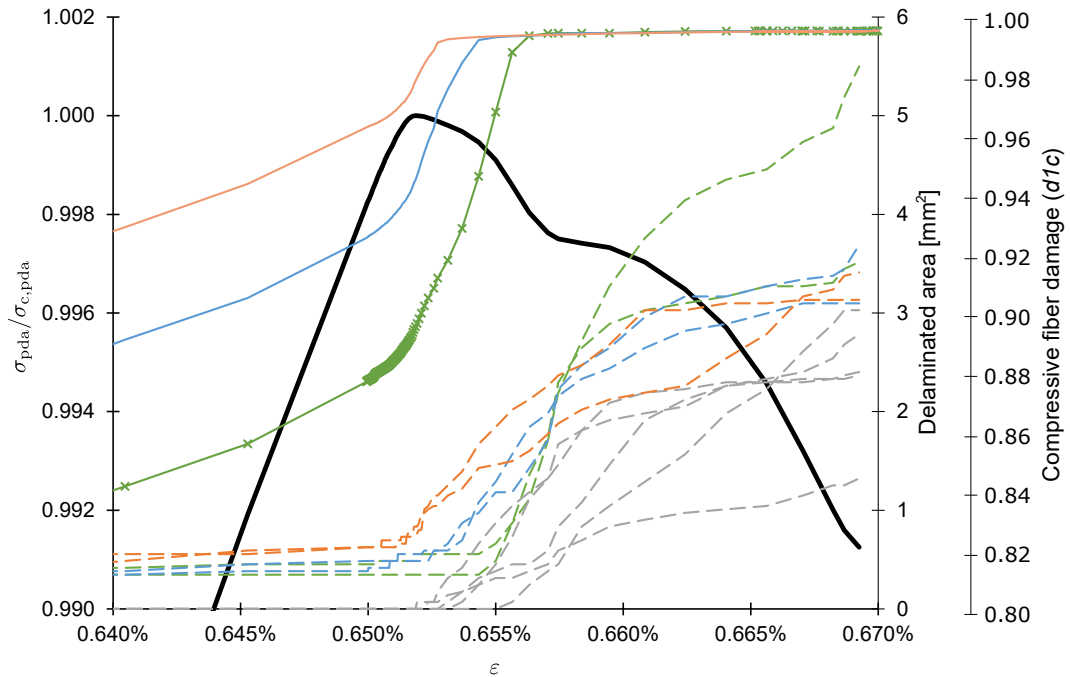

Figure 15: Normalized stress (solid black line), fiber damage (solid colored lines), and delaminated area (dashed lines) vs. nominal strain from the Quasi 0.2 mm mesh size model in the vicinity of the predicted peak load.
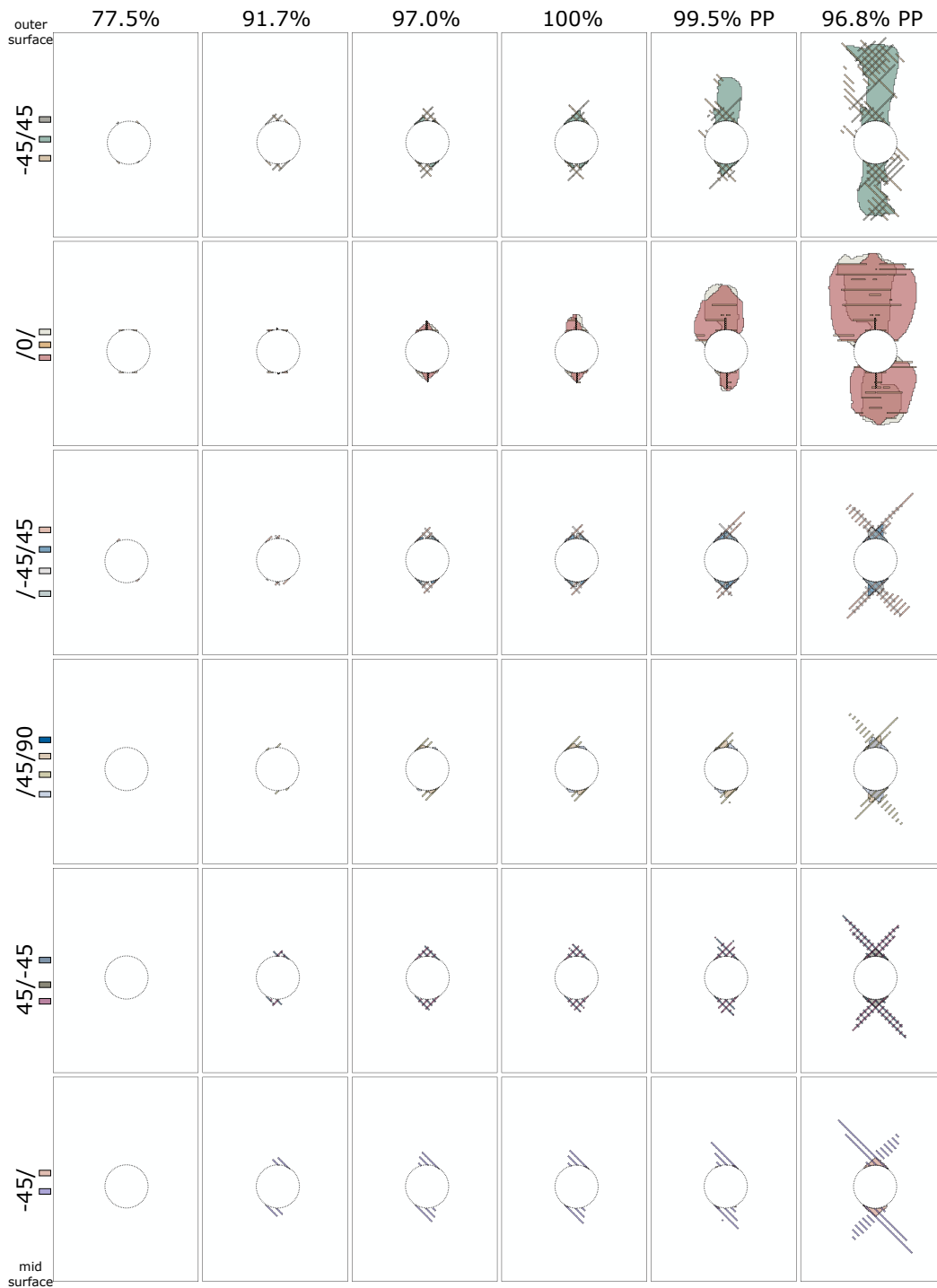
31

Figure 16: Deformed cross section of the Quasi laminate at the 97% post-peak load level predicted by the 0.2 mm mesh model. The arrows point to localized fiber damage.

4.2.3 Damage evolution in the Soft laminate

The damage states predicted for the Soft layup are shown in Figure 17, using the same format described previously. In contrast to the results for the Hard and Quasi laminates, the predicted pre-peak damage state for the Soft laminate is relatively large, extending about 2.5 mm from the hole, and multi-modal. The pre-peak damage states include matrix cracks tangent to the hole, small delaminations at several interfaces bounded by matrix cracking planes, and fiber damage in the 0° plies. At the peak load, the damage state resembles the same pattern seen at 97% load, with the matrix cracks, fiber damage, and delaminations all propagated by a small amount. Interestingly, after the strength is reached, the fiber damage zone in the 0° plies remains about the same length as it was at the pre-peak 97% load level. This is in contrast to the damage evolution predicted in the Hard and Quasi layups, where the fiber damage grows significantly after the peak load is reached. Large delaminations develop at the first three ply interfaces, two of which neighbor the 0° plies. The plies interior to the 0° ply exhibit primarily matrix cracking with some relatively small delaminations. The results shown in Figure 17 suggest that sub-laminate buckling is more important to the overall load carrying capability of the Soft layup than fiber damage.

The results shown are for the 0.2 mm mesh size. The damage sequences for the Soft layup predicted using the 0.15 and 0.25 mm meshes were similar with slightly less delaminated area predicted in both cases.

As was presented for the other layups, the details of the failure sequence near the peak load are shown in Figure 18. The stress-strain curve is the thick black line plotted using the left ordinate, where the final 10% of the response is shown, which is a significantly broader range than was shown in Figure 10 and Figure 15. In

Figure 17: Analysis predicted damage states at several load levels for the Soft layup. The load of each image is shown across the top as $\sigma_{\mathrm{pda}}/\sigma_{\mathrm{c,pda}}$ (PP indicates post-peak), and the ply group is labeled along the left.

the Soft laminate, the failure sequence occurs over a much larger range of load and strain than in the other two laminates. The maximum fiber damage variable ($d1c$) value in the 0° ply is the solid blue line, plotted using the right-most ordinate. The dashed lines are the cumulative delaminated area for each ply interface. Only half of the ply interfaces are shown for clarity, since the delaminated area was relatively symmetric about the mid-thickness plane of the specimen. Two delaminated area curves are colored blue to indicate these are the interfaces adjacent to the 0° ply, with the lighter blue curve corresponding to the inner interface. The outermost interface result is colored in orange and the remaining interfaces are shown in gray. The results show an increase in both fiber damage and delaminated area at 0.73% strain, which coincides with a load drop in the stress-strain curve. At this point the fiber damage extends to roughly the configuration shown at the 97% load level in Figure 17, with the maximum value being about 0.99. As the strain is increased, the load also increases beyond the previous peak. Apparently, enough load transfer occurs to the ±45° plies to sustain further loading despite the damaged 0° plies. As the load increases between 0.74% and the peak at 0.78% strain, there is some decaying oscillation in the stress-strain curve, which is a result of dynamic vibrations from the damage event at 0.73% strain. The default damping in the quasi-static explicit dynamic analysis is responsible for the decay in the vibrations. When the strength is reached, large delaminations develop at three ply interfaces. Two of three interfaces are those neighboring the 0° ply. The third interface is the only other interface external to the 0° ply. At the same time, the fiber damage increases by only a small amount, about 0.005, which corresponds with a few percent increase in dissipated energy. Therefore, the strength is reached when the laminate experiences sublaminate buckling of the outer ±45/0 ply group. Considering these results together, the predicted failure sequence is: 1) first fiber damage in the 0° ply that causes a small load drop, but is arrested by load transfer to the ±45° plies, 2) delamination at the interfaces adjacent to the 0° plies grows, and then 3) sub-laminate buckling occurs. The same caution given regarding sublaminate buckling in the Hard laminate is repeated: it is noted that with one C3D8R element through the thickness of each ply, the bending stiffness of the delaminated plies is inaccurate and therefore the sub-laminate buckling response should be examined further.

The analysis predicts a load drop prior to reaching the peak load, which is qualitatively in agreement with the test measurements since they show small load drops at around 90% of the peak load. However, in the test results, after the initial load drop, a loss of stiffness occurs and significantly more compressive strain is needed to reach the peak load. In the analysis result, the stiffness is retained after the load drop and only a small increment in strain (0.04% strain) is need to fail the coupon.

A cross section view showing the deformed state of the plies at the 99.5% post-peak load level is shown in Figure 19. The elements where fiber damage has localized in the 0° plies are indicated with arrows. As in the other layups, it is noted that the fiber damaged elements have sheared out-of-plane and that large open delaminations developed adjacent to the fiber damage. The same view of the model at the 96.8% post-peak load level (not shown) has similar deformations with greater amplitude.
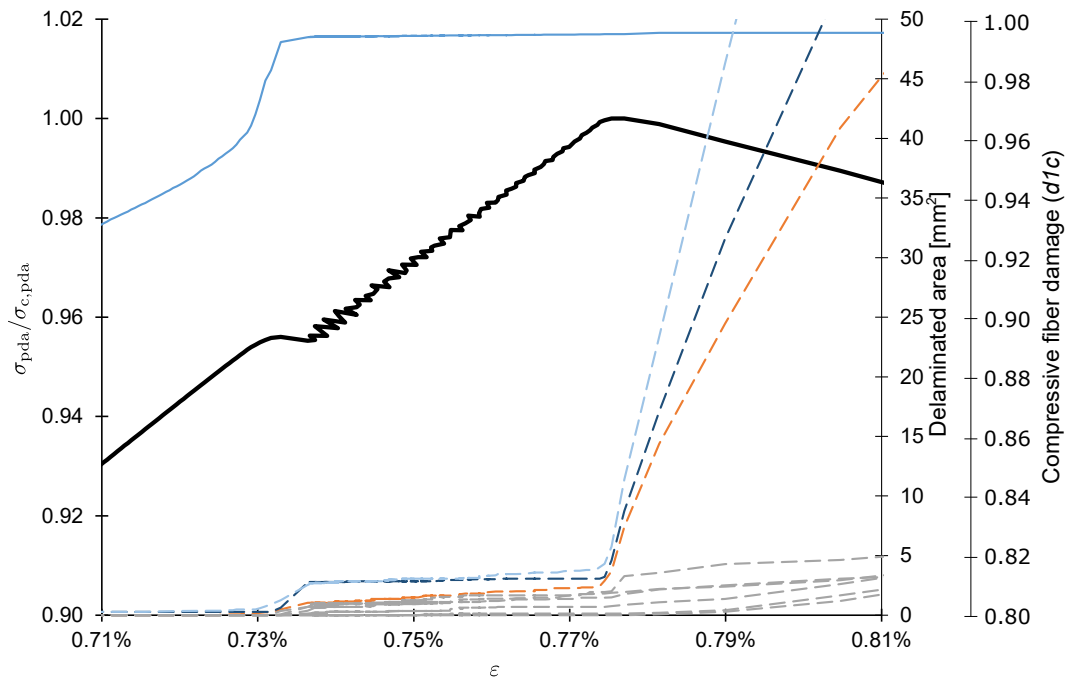
Figure 18: Normalized stress (solid black line), fiber damage (solid blue line), and delaminated area (dashed lines) vs. nominal strain from the Soft 0.2 mm mesh size model in the vicinity of the predicted peak load.
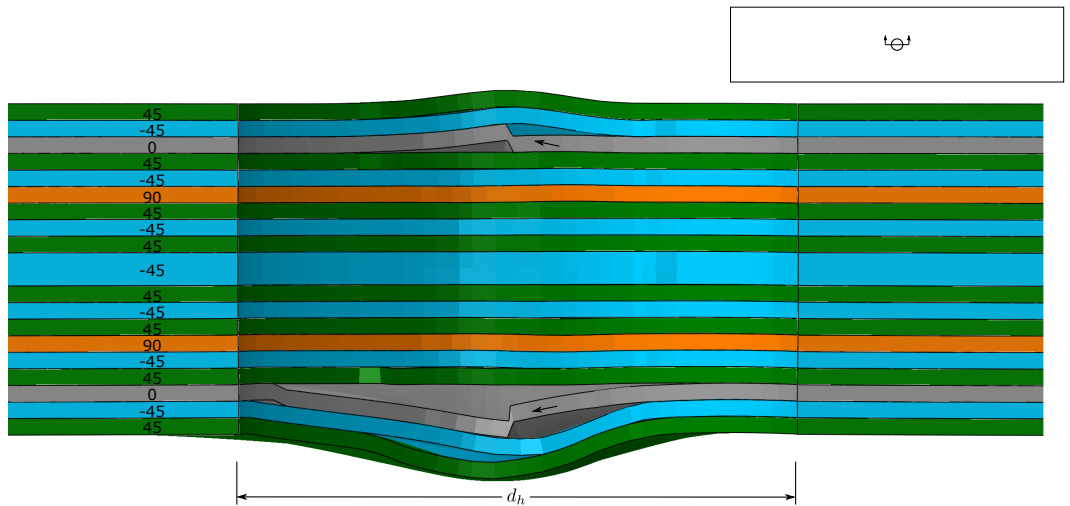

Figure 19: Deformed cross section of the Soft laminate at the 99.5% post-peak load level predicted by the 0.2 mm mesh model. The arrows point to localized fiber damage.

4.3 Comparison of measured and predicted damage states at 75% and 90% load levels

A direct comparison between the measured and predicted damage states is shown in Figure 20. The comparison is constructed by overlaying the analysis results on the observations from X-Ray CT that were shown previously in Figure 5. Analysis results from the models with the 0.2 mm mesh size were extracted at the output frame closest to the 75% and 90% load levels used for the tests. In the case of the Soft layup, the analysis peak load occurs at 89.2% of the test average, so the frame at peak load is used in the comparison. In the other cases, the analysis results are extracted within 0.5% of the target load level. The analysis results show the projection of matrix cracking and fiber compression damage as the superposition of the maximum extent of damage in each ply. The analysis results are shown by the translucent regions, having a width equal to element size. The damage is colored by mode as follows: green for $+45°$ matrix cracks, red for $0°$ matrix cracks, teal for $-45°$ matrix cracks, and blue for $0°$ fiber compression damage. The predicted delaminations (see Figures 9, 14 and 17) are not shown for two reasons: 1) no delamination was found in the X-Ray CT data and 2) to reduce clutter in the figure. Overall, the predicted damage states in the $0°$ plies are in reasonable agreement with the test measurements. However, the agreement in the $\pm45°$ is generally not very good. Matrix cracks tangent to the hole are predicted in the $\pm45°$ plies, however, no corresponding cracks were found in the test observations. The correlation of the predicted and measured damage states is discussed for each layup in the following paragraphs.

Considering the Hard laminate, the analysis over-predicts splitting crack lengths in the $0°$ plies at 75% but then under-predicts the length of two of these cracks at 90% load. Short matrix cracks (< 1 mm) in the $-45°$ plies adjacent to the central $0°$ ply block are seen in both the test and analysis results. The overlay shown here highlights that although the pattern is similar, the model does not have sufficient resolution to reproduce the observed crack spacing. The $-45°$ matrix cracks occur very close to each other in the test. The analysis also disagrees with the test results in that matrix cracking is predicted to the left and right of the holes, due to local tension from Poisson's effect. No damage was found in these regions in the test observations. Overall, the damage comparison shows partial agreement at both the 75% and 90% load levels. The differences are likely due to both insufficient ability to resolve closed cracks in the test measurements and shortcomings of the model.

In the Quasi laminate, the analysis results show some short (about 1 mm) matrix cracks at the 75% load level. No damage was visible in the X-Ray CT results after the specimen was subjected to this load level. The short lengths of the predicted cracks are on the order of the minimum detectable crack size in the X-Ray scans. At the 90% load level, both test and analysis results show splitting cracks in the $0°$ plies, with the analysis slightly over-predicting the crack lengths. For the Quasi laminate, there is partial agreement between test and analysis results for both load levels. The 75% load level is considered to be in partial agreement since the predicted crack lengths are very short.

The results for the Soft laminate show relatively good agreement for the $0°$
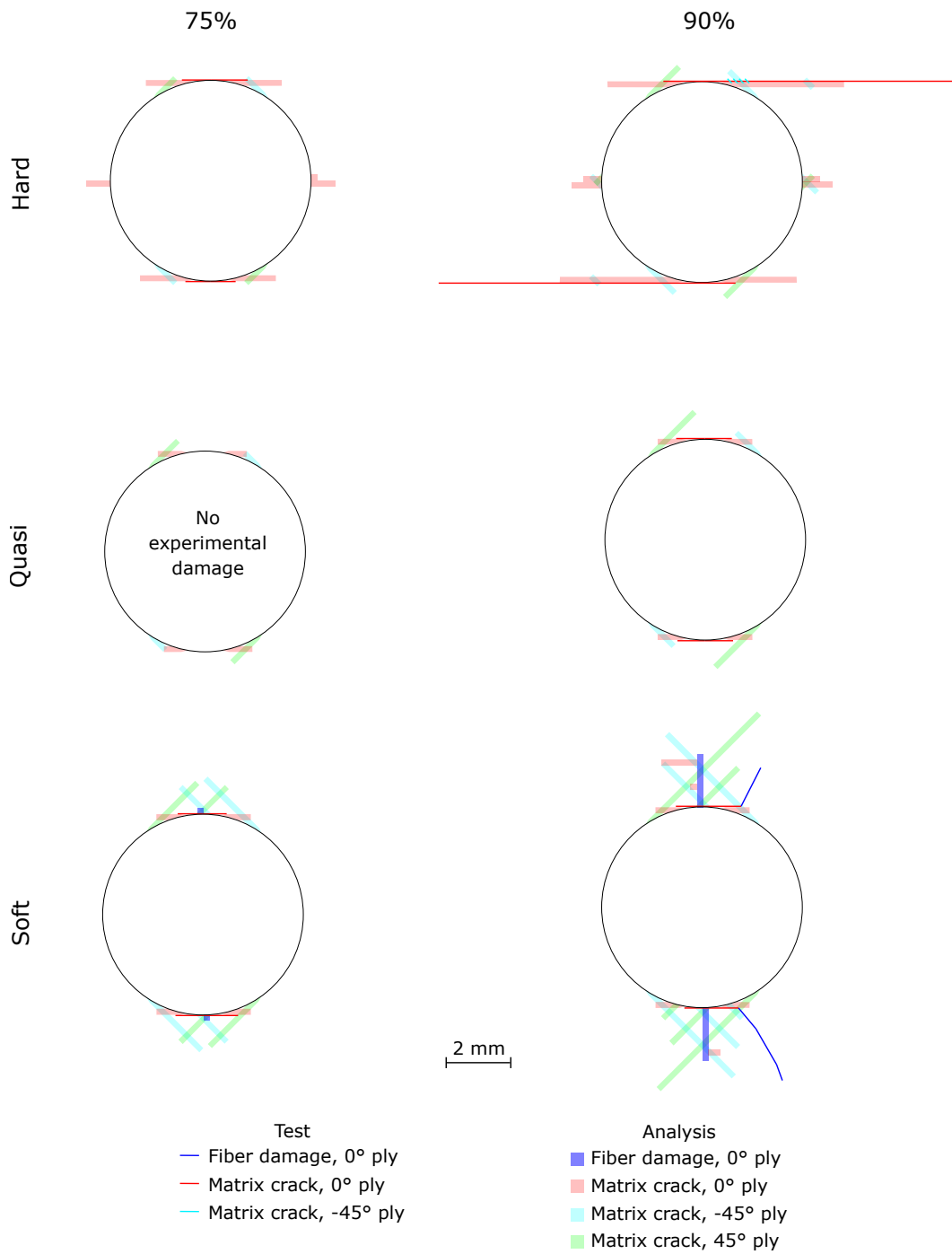
Figure 20: Comparison of measured and predicted damage states. The damage is colored by mode as follows: green for +45° matrix cracks, red for 0° matrix cracks, teal for −45° matrix cracks, and blue for 0° fiber compression damage.

plies in terms of the length of both matrix cracking and fiber compression damage. Although the fiber damage threshold ($d1c \geq 0.9$) was selected arbitrarily, the length of the fiber damage zone predicted by the analysis is in good agreement with the test results. The model cannot predict the abrupt onset of fiber damage observed via DIC; instead, a relatively gradual fiber damage process is predicted. The fiber damage observed in the test occurs at the end of splitting cracks and propagates at roughly 60° from the loading direction. The analysis predicts that fiber compression damage initiates and propagates from the stress concentration next to the hole, such that the location is not in good agreement between test and analysis. Since the model calculates fiber damage onset using only the longitudinal strain, it is unable to predict fiber damage that occurs at the end of splitting cracks. The main discrepancy in the predictions for the Soft laminate as compared with the X-Ray observations is that the analysis predicts extensive matrix cracking in the ±45° plies while no cracks were observed in these plies in the test data.

4.4   Summary of test and analysis comparison

A high-level summary of the comparison between test and analysis results is provided in Table 5. For the initial stiffness, strength, and strain-to-failure, the analysis result is quantified in terms of percent error from the average test result. The agreement between the test and analysis at the 75% and 90% load levels are qualified as poor, partial, or good. Results are tabulated for all three mesh sizes. The summary emphasizes that the agreement in terms of the stress vs. strain response is generally very good. For the Quasi and Hard layups the errors in stiffness, strength, and strain-to-failure are all below 5% for the 0.15 mm mesh size. For these layups, the agreement between test and analysis improves as the mesh size reduces, which gives confidence in the modeling approach. The aforementioned differences in the predicted and observed damage evolution in the Soft layup is reflected here in generally worse overall agreement, especially in terms of strain-to-failure. The qualitative assessment of the damage states shows partial agreement for most cases with the exception being the Soft 90% load level, which is rated as poor. The assessment of agreement in damage states reflects both potential inaccuracies of the model as well as potentially insufficient inspection resolution since in many cases the analysis predicted small cracks (< 1 mm long) that were not observed in the X-Ray CT results.

Table 5: Summary of analysis results in terms of selected quantitative and qualitative metrics.

Layup	Mesh size	Initial stiffness	Strength	Strain-to-failure	Damage 75%	Damage 90%
Hard	0.25	-3.6%	-10.7%	10.4%	partial	poor
	0.20	-3.6%	-5.8%	-5.2%	partial	partial
	0.15	-3.7%	2.8%	3.8%	partial	partial
Quasi	0.25	0.6%	-3.8%	-7.7%	partial	partial
	0.20	0.5%	-3.9%	-9.0%	partial	partial
	0.15	0.5%	1.8%	-3.1%	partial	partial
Soft	0.25	-0.5%	-8.2%	-29.8%	partial	poor
	0.20	-0.5%	-10.3%	-31.1%	partial	poor
	0.15	-0.5%	-11.9%	-33.1%	partial	poor

4.5 Interactions between fiber damage and delamination

The analysis results show that delamination plays a role in the predicted strength for all three layups. In the Quasi and Soft laminates, delamination and subsequent sub-laminate buckling contribute to the predicted loss in load carrying capability. For all three laminates, the delaminated area increases with fiber damage, continuing to increase after the fiber damage plateaus (Figures 10, 15 and 18). The cross-section images of the deformed mesh (Figures 11, 16 and 19) indicate that out-of-plane shearing occurs in the elements where fiber damage localized. Considering these observations, the models appear capable of accounting for the interaction between compressive fiber damage and delamination, wherein compressive fiber damage drives delamination which may eventually lead to sub-laminate buckling.

While the prediction of fiber compression and delamination interaction is physically relevant, it is surprising that the model is capable of predicting this behavior. The constitutive model softens the fiber direction response and has no direct effect on the other terms of the stiffness matrix (i.e., G_{13} is not degraded). Therefore, the constitutive model suggests that increasing fiber compression damage would cause the element to progressively flatten, without any noticeable effect on its shear or out-of-plane response through the damage evolution.

However, in the presence of a small shear deformation, the material coordinate system may become slightly misaligned, resulting in non-negligible shear stresses. Such material system rotation explains how large out-of-plane stresses may develop in the solid elements representing the plies, that force delamination onset and propagation. Notionally, out-of-plane deformations are equally likely to occur whether or not the element experiences fiber damage since, as noted above, the constitutive model does not affect these stiffness terms. However, the numerical controls (e.g. enhanced hourglass control and distortion control) that prevent large changes in element volume, introduce a perturbation that promotes shearing deformations. Thus, one reason why the large out-of-plane shearing localizes in the fiber damaged elements is numerical issues associated with large deformations and large decrease in volume. Further investigation of this observation is needed to clarify the material
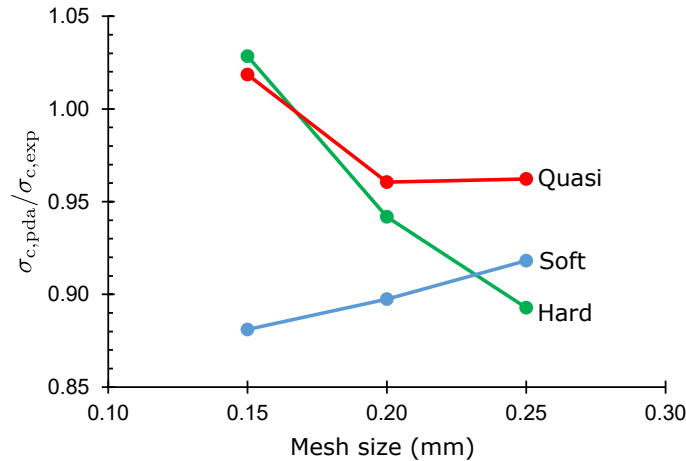
Figure 21: Predicted strength normalized to the measured strength as a function of mesh size.

modeling, discretization, and numerical considerations.

5 Effect of numerical parameters

The effects of two numerical parameters (mesh size and mass scaling) on the predicted results are examined in this section. First, the effect of mesh size and the mesh convergence of the results are discussed. Then, the role of mass scaling is described and evaluated.

The stress vs. strain results for the three mesh sizes considered (0.15, 0.2, and 0.25 mm) were presented previously in Figure 8. In general, the responses from the different mesh sizes are very similar. To evaluate the mesh convergence, the predicted strengths normalized to the average experimentally measured strength are plotted as a function of the mesh size in Figure 21. The results are somewhat inconclusive in terms of mesh convergence; additional mesh sizes are needed for this evaluation. However, the results for the Hard and Quasi laminates approach the experimental averages as the mesh size is reduced. It is interesting that the error in predicted strength reduces when the mesh size is reduced from 0.2 to 0.15 mm, since previous verification and benchmarking studies have suggested that 0.2 mm mesh size is sufficiently small to predict matrix cracking accurately for this material system [18]. The difference in the trend for the Soft layup may reflect the fact that its strength prediction is more sensitive to sub-laminate buckling than fiber damage. While conducting analyses with additional mesh sizes may help elucidate the mesh convergence characteristics of the current model, no further analyses were conducted because reducing the mesh size below 0.15 mm was computationally intractable and increasing the mesh size above 0.25 mm is known to produce inaccurate results for matrix crack propagation [18].

Several analyses were run with varying amounts of mass scaling to examine the

sensitivity of the results to the mass scaling settings. As the amount of mass scaling was reduced, the results converged for the three mesh sizes and three different layups. The final values (nominal values reported in Section 3) used for mass scaling led to converged results in terms of the stress vs. strain results and damage evolution.

Prior to conducting the mass-scaling convergence study described above, the common rule-of-thumb, wherein an analysis result is considered sufficiently quasi-static if the overall kinetic energy is less than a certain fraction of the internal energy (e.g., 1%) was used as a baseline. Relatively large amounts of mass scaling, wherein the final result is obtained in less than 2×10^5 increments, satisfy the 1% kinetic energy heuristic, but produce noticeable oscillations in the stress-strain curves. Only by detailed examination of the results for evidence of dynamic effects was it possible to conclude the results are relatively quasi-static. It is noted that artifacts of the mass scaling do remain (e.g., the oscillations after the load drop in Figure 18), but in general are very small. Since the final outcome of the mass-scaling convergence study was that about 1.5×10^6 increments were needed to obtain a quasi-static solution, and the maximum allowed number of increments in a double precision Abaqus/Explicit analysis is 2×10^6, when possible it may make more sense to simply attempt to use as many increments as possible to get the most quasi-static result possible instead of trying to optimize the mass scaling parameters.

6 Sensitivity to physical parameters

In light of the overall good agreement in predicted and measured strength, the sensitivity of the models was evaluated with respect to selected physical parameters. First, the effect of thermal residual stresses is considered. Then, the effect of the parameters that define the compressive fiber constitutive response are evaluated.

6.1 Effect of considering thermal residual stresses

While many analyses ignore thermal residual stresses, in certain situations they can be important. Analyses were conducted to evaluate the effects of thermal residual stresses on the predicted damage evolution and stress vs. strain response for the three laminates. Thermal residual stresses were modeled by assigning coefficients of thermal expansion to the plies and applying an initial prescribed temperature drop ΔT in a thermal cool down step. The prescribed displacement was then applied subsequently in the loading step.

In terms of the overall stress vs. strain response shown in Figure 22, the inclusion of ΔT had different effects depending on the layup. In the figure, the stress vs. strain responses from the baseline are shown with the solid dark-colored lines and the responses from the analysis using the thermal step are shown with the dashed lines. The test data are shown with the light-colored lines. The response for the Hard layup[6] was nearly identical with and without the thermal step. For the other two layups, significant differences are noted in the response. In all cases, the pre-

---

[6]The Hard layup analyses were conducted with the 0.15 mm mesh size. The other two layups were analyzed with the 0.2 mm mesh size.
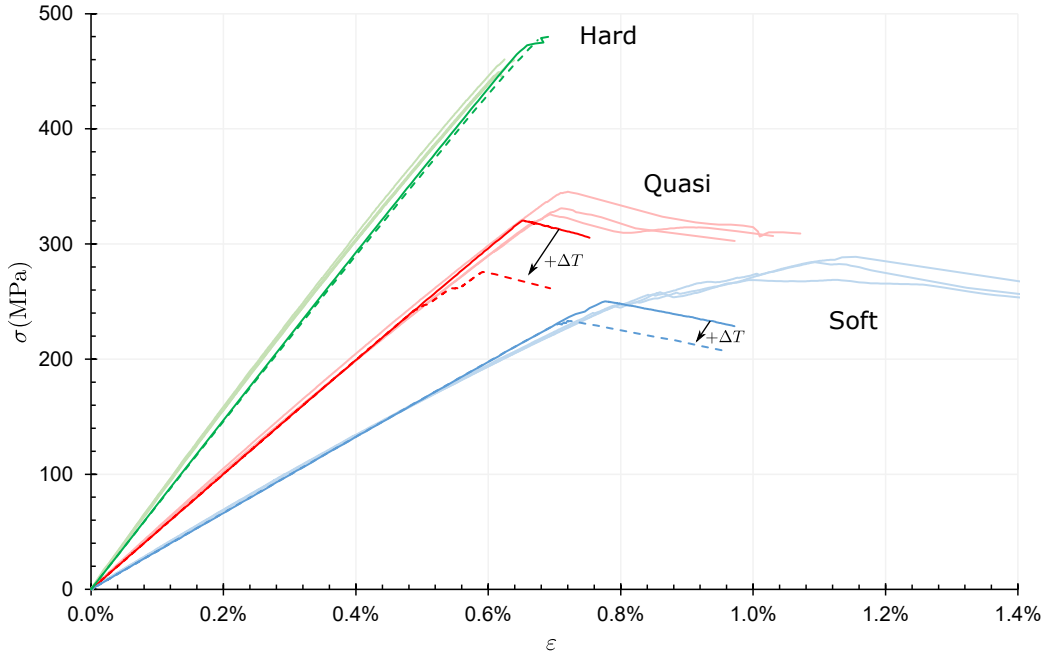
Figure 22: Stress vs. strain with (dashed lines) and without (solid lines) thermal residual stresses. The light colored lines are the test results.

dicted strength is reduced when the thermal step is included. Considering the test data, it is noted that the agreement between test and analysis deteriorates when the thermal step is included. While it is presumed that adding the thermal step should decrease the predicted error compared with experiments, several potential explanations for alternative behavior are available. First, some material properties measured using laminates (e.g. G_{FC}) implicitly include the effects of thermal residual stresses, resulting in double counting the thermal residual stresses. In addition, the specimens may have absorbed some moisture, which relieves the thermal residual stresses [39]. The moisture level of the specimens was not monitored. Finally, the linear thermal step may be overly simplistic considering the residual strains result from a complicated nonlinear material process.

The differences in the damage evolution from the simulations with and without the thermal step are discussed in the remainder of this section. First, the large differences in stress vs. strain response are explained in terms of the damage evolution behavior for the Soft and Quasi laminates. Then, the results for the Hard laminate are shown.

The damage evolution predicted by the models with and without thermal residual stresses is summarized in Figure 23 for the Soft and Quasi laminates. The results shown in blue are the baseline analysis results and the curves shown in red are the analysis results including the thermal step. The delaminated area averaged across all of the ply interfaces is shown with the dashed lines plotted using the left-hand ordinate. The maximum value of compressive fiber damage throughout the model

42
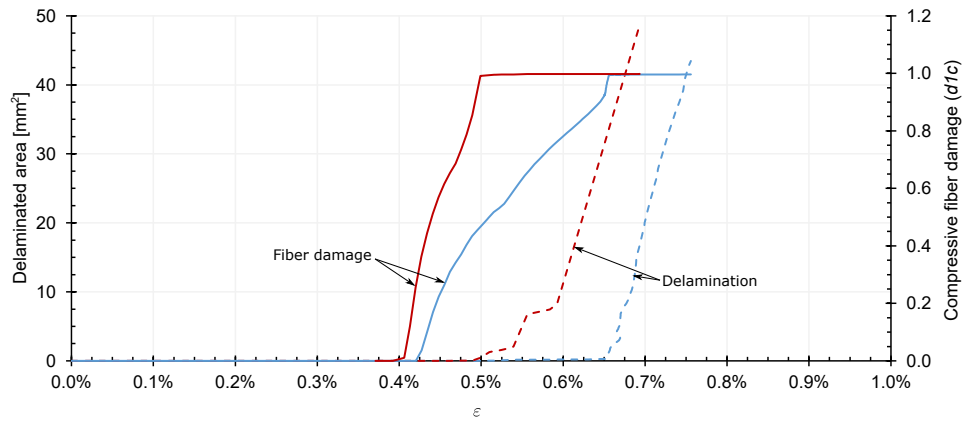
(a) Quasi layup.
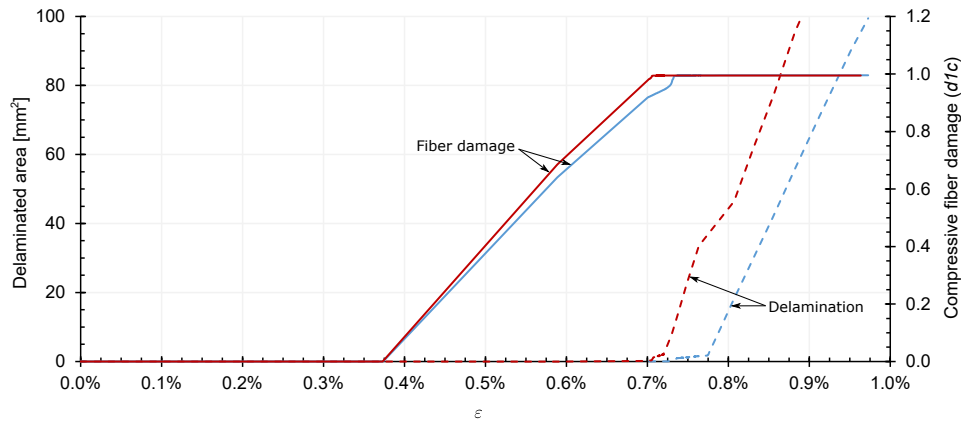
(b) Soft layup.

Figure 23: Effect of thermal residual stresses (red lines) on the fiber compression damage and delamination evolution. The blue lines are the baseline results without thermal residual stresses.

is shown as a function of applied strain with the solid lines plotted using the right-hand-side ordinate axis. For the Quasi layup, when thermal residual stresses are included the fiber damage is nearly double that without thermal stresses at 0.5% strain. Likewise, the rapid increase in delaminated area occurs at about 10% lower strain when thermal stresses are included. In the result with the thermal step, the peak load occurs around 0.6% strain, which is well after the fiber damage has plateaued and when the delamination area is becoming large. This is in contrast to the baseline result, where it was found that the peak load occurs when the fiber damage and delaminated area are both growing. Hence, when adding thermal residual stresses, the Quasi layup strength becomes controlled by sublaminate buckling. For the Soft laminate, the differences between the two analyses were smaller. With and without the thermal step, the failure mode is sublaminate buckling. The main differences between the two models is that, when the thermal step is included, the delaminated area increases at a lower applied strain level.

The damage pattern for the Hard laminate is very similar with and without the thermal residual stresses, consistent with the stress vs. strain response. However, the inclusion of thermal residual stresses changes the propagation rate of the splitting cracks in the central $0°$ ply block. The nominal analysis results differ greatly from the measured split lengths at the 90% load level (see Figure 12). To investigate how thermal residual stresses change the split propagation behavior, a series of analyses were run for the nominal temperature change from the cure cycle information, $\Delta T = -155°C$, and several lesser values to survey the sensitivity of the splitting crack propagation to ΔT. To ensure that the splits do not reach the end of the damageable region, the local PDFA region was extended from 20 mm to 30 mm. The 0.15 mm mesh size model was used for this study. Due to a memory limitation in the Abaqus/Explicit packager[7] related to the very large number of degrees of freedom of these models, the model width was reduced from 38.1 mm to 30 mm. The results are shown in Figure 24 alongside the analysis with no thermal cool down ($\Delta T = 0°C$) and the test measurements repeated from Figure 12. At locations B and C shown in Figure 24a, the test measurements show the splits are about 1-mm-long at 0.46% strain (75% load) and grow to about 8 mm by 0.56% (90% load). The nominal analysis result with no thermal residual stresses agrees with the test data at 75% load, but underpredicts the split length by about 50% at the 90% load level. Adding thermal residual stresses results in unstable propagation of the splitting cracks shown by the vertical jumps in the curves for $\Delta T = -60°C$, $-100°C$, and $-155°C$. The analysis result using $\Delta T = -155°C$ matches the split length at the 90% load level, but overpredicts the split length at the 75% load level. No analysis result matches the test data at both load levels. While further investigation is needed to understand this discrepancy, one potential explanation is scatter (replicate-to-replicate variations) in the test data since the test measurements at 75% and 90% load levels were made using two separate specimens. Considering the splitting crack lengths at locations A and D in Figure 24b, the results are generally insensitive to ΔT at the 75% and 90% load levels.

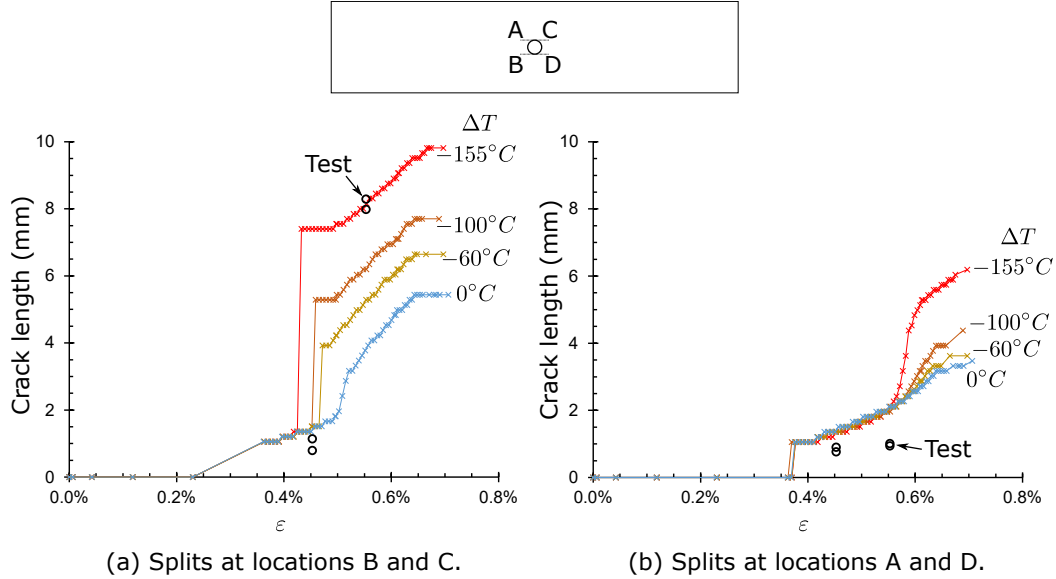[7]Abaqus software developers are aware of this limitation and intend to fix it in a future release.

Figure 24: Splitting crack lengths in the central 0° ply block in the Hard laminate vs. strain showing the effect of different values of ΔT.

6.2 Effect of X_C

The longitudinal compressive strength, X_C, is challenging to measure, see e.g. [40]. The nominal value $X_C = 1731$ MPa used in this work comes from [33]. This value is high compared with other values of X_C reported in the literature for IM7/8552. For example, $X_C = 1200$ MPa is reported in [41]. Lee and Soutis showed a thickness sensitivity, with X_C reported between 869 and 1570 MPa, which they correlated with initial fiber misalignments [7]. It is noteworthy that the X_C calculated based on multidirectional laminate tests in [7] is 1710 MPa, very similar to the value used herein, reported in [33]. Following [7, 40], it is argued that the lower values of X_C are an artifact of test method issues (e.g. stress concentrations at the tabs) and that the higher value is the representative strength that should be used. Nonetheless, analyses were run with the 0.2 mm mesh models using $X_C = 1200$ MPa and compared with the nominal results to quantify the sensitivity of the model predictions to the longitudinal strength.

The stress vs. strain curves for the two strength values and each layup are shown in Figure 25. The nominal results with $X_C = 1731$ MPa are repeated from Figure 8 and shown with the dotted lines. The results with $X_C = 1200$ MPa are shown with the solid lines. Almost no sensitivity to X_C is seen for the Quasi layup, while pronounced differences are noticed for the other two layups. The results obtained for the Hard and Soft layups with the two values for X_C are discussed in the remainder of this section.

For the Hard laminate, $X_C = 1200$ MPa reduces OHC strength because fiber damage starts earlier and leads to large delaminations at the first load drop. The eventual collapse is still governed by fiber damage, but delaminations play a larger
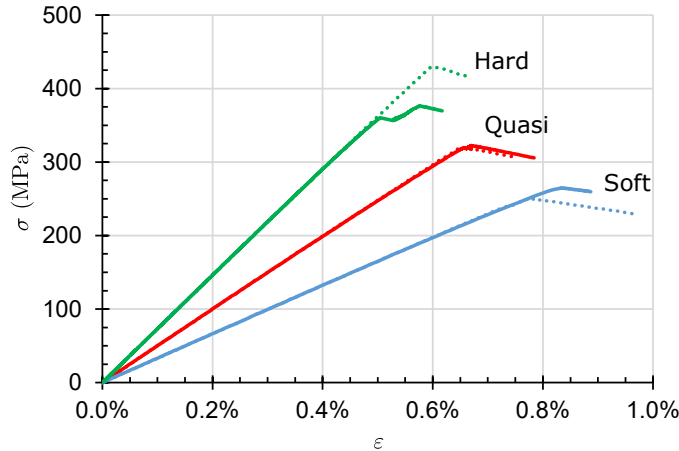
45

Figure 25: Stress vs. strain for the nominal 0.2 mm mesh models with $X_C = 1731$ MPa (dotted lines), and the same models with $X_C = 1200$ MPa (solid lines).

role in that they result in more load transfer into the zero plies. The failure mechanism resembles the nominal Quasi laminate failure mechanism, where there is an interaction between fiber damage and delamination. This is in contrast to the nominal Hard laminate failure sequence, which is dominated by fiber compression failure. In addition to the reduced strength, there is a compounding factor that further amplifies the difference in load at onset of fiber damage when using the reduced X_C. When X_C is reduced, the splitting cracks in the $0°$ plies are relatively short at fiber damage onset. When X_C is increased, the splitting cracks propagate farther prior to fiber damage onset, thus blunting the longitudinal stress concentration, which in turn delays the fiber damage. In summary, the Hard laminate results are sensitive to X_C in terms of when and how damage evolution occurs.

The fiber damage predicted in the Soft laminate for $X_C = 1200$ MPa exhibits a non-physical pattern that results from numerical deficiencies of the model. The observed fiber damage pattern near the peak load is shown in Figure 26a. The alternating rows of damaged and undamaged elements is a pattern resulting from a numerical issue and is not physically relevant. This spurious damage pattern may arise due to the combination of process zone size and local stress state, but once the pattern starts with damaged-undamaged-damage elements at the hole boundary it is self-propagating. The results for the simulation using the nominal material properties did not exhibit this spurious damage pattern. The fracture process zone size l_{FPZ} is proportional to $E_{11}G_{FC}/X_C^2$ (see, e.g., [35]), whereby it is clear that arbitrarily reducing the X_C as done here increases the process zone length. Holding the process zone length constant, if $X_C = 1200$ MPa, then $G_{FC} = 29.3$ kJ/m^2. Reducing the strength and toughness using a constant l_{FPZ}, the same spurious damage pattern appears, but the damage is mostly concentrated in the center row of elements as shown in Figure 26b, so the result is not completely satisfactory. Although not implemented, one simple way to circumvent this numerical issue is to
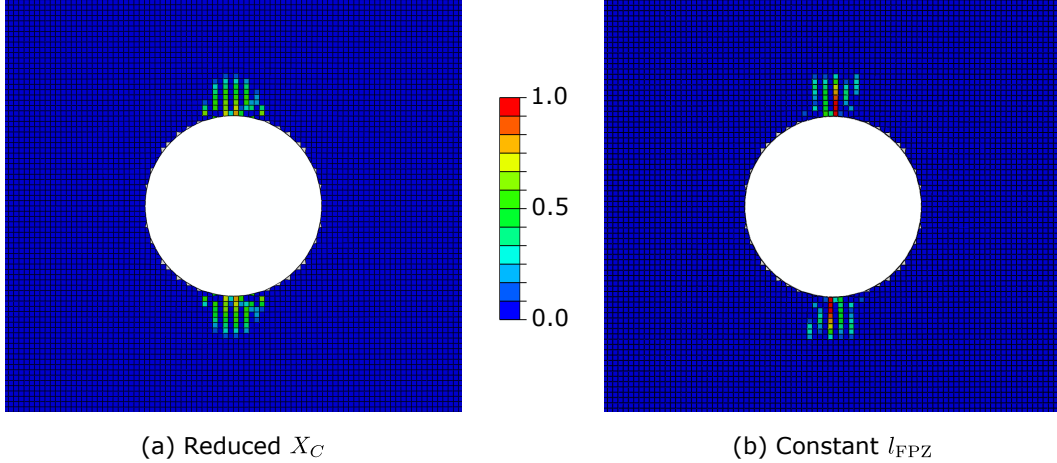
(a) Reduced X_C (b) Constant l_{FPZ}

Figure 26: Spurious fiber damage pattern in the results for the Soft laminate showing alternating rows of damaged elements. The results are shown at 77.6% $\sigma_{\mathrm{c,pda}}$.

enforce a minimum crack spacing with 2 or more undamageable elements between each row of damageable elements using the section definition as is done for matrix cracking. In light of the numerical difficulty encountered in the Soft laminate for $X_C = 1200$ MPa, the predicted response is not considered trustworthy. These results are shown to underscore the challenges in developing PDFA models that are robust across a practical input parameter space.

6.3 Effect of G_{FC}

The sensitivity of the results to the fiber fracture toughness G_{FC} is interesting to investigate since there is no consensus or test standard for measurement of this material input. The particular nominal value used in this study, $G_{FC} = 61$ kJ/m^2 was measured using a series of geometrically-scaled cross-ply double edge notched specimens in [34]. During the ACP, these tests were repeated using the same material and processing procedures as used to fabricate the OHC specimens. The fracture toughness was found to be $G_{FC} = 57.1$ kJ/m^2 [36], very similar to the value reported in [34]. Others have generally reported a wide range of values for G_{FC}, all lower than the value found from the double edge notch tests. Catalanotti et al. tested cross-ply compact compression specimens made from IM7/8557 and reported $G_{FC} = 47.5$ kJ/m^2 [42]. Laffan et al. [43] and Wind et al. [44] used notched unidirectional four-point-bend specimens made from IM7/8552 and report much lower values: 25.9 kJ/m^2 and 28.3 kJ/m^2, respectively. Catalanotti et al. say that the rising R-Curve explains the wide range of reported values in that the lower values are simply points lower on the R-Curve than the higher values [34].

The sensitivity of the predicted strength to different values of G_{FC} was analyzed for all three layups and the results are shown in Figure 27. Three off-nominal values of G_{FC} were considered: 30, 45, and 75 kJ/m^2. The computed strength ($\tilde{\sigma}_{\mathrm{c,pda}}$) is normalized by the nominal predicted strength on the ordinate axis. In general, a
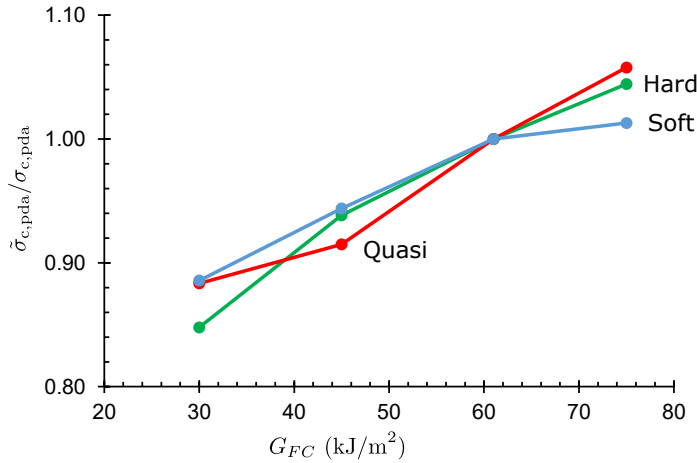
Figure 27: Sensitivity of the predicted strength to G_{FC}.

consistent trend is observed with higher values of G_{FC} producing higher predicted strengths. It is noteworthy that using $G_{FC} = 30$ kJ/m^2 to represent the lower reported values reduced the predicted strength by 10–15%. Since the predicted strengths are generally below the measured strengths, the expected error compared with the experiments when using the lower values of G_{FC} is in the range of 10–20%.

The role of fiber damage in the failure sequence explains some of the details in the results shown in Figure 27. The Hard and Quasi laminates are more sensitive than the Soft laminate to G_{FC}, which is expected since the Soft laminate failure is primarily driven by sub-laminate buckling. However, the Soft laminate has some sensitivity to reduced values for G_{FC}. Decreasing G_{FC} leads to earlier and more extensive fiber damage, which promotes earlier and increased delamination, which in turn makes sub-laminate buckling more likely. The Quasi laminate result shows a noticeable knee in the curve where the knockdown from 45 to 30 kJ/m^2 is much less than from 61 to 45 kJ/m^2. This occurs because at 30 kJ/m^2 the failure mechanism changes to sub-laminate buckling.

7   Concluding remarks

This report describes a recent validation activity conducted as part of the NASA Advanced Composites Project (ACP) to evaluate the capability of the progressive damage analysis code CompDam for predicting OHC failure. Tests were conducted on OHC specimens with three different layups using digital image correlation and X-Ray computed tomography to help capture the structural response and damage evolution. The experimentally observed failure mechanisms were found to be similar to those reported in the literature. The experimental measurements of damage states were synthesized into schematic damage maps to facilitate understanding and comparison with analysis predictions.

Finite element models of the OHC specimens were constructed for use with the

CompDam material model. The fiber direction compression response was modeled using a conventional continuum damage mechanics approach with a trilinear stress-strain law. Detailed interrogation of the analysis results and comparisons with experimental measurements provided a basis for assessing the capability of the models. Evaluation of the model results elucidated the role of the matrix cracking, delamination, and fiber compression damage and their contribution to structural collapse. Based on the study, several conclusions and comments are enumerated.

1. The test and analysis structural responses are generally in good agreement in terms of stiffness, strength, and strain-to-failure. With the smallest mesh size (0.15 mm), the error in predicted strength is 2.8%, 1.8%, and -11.9% for the Hard, Quasi, and Soft layups, respectively.

2. The strain-to-failure is not well predicted in the Soft laminate, apparently because the model does not capture well the residual loading capability after fiber damage initiates. This finding highlights the importance of using a range of laminates in validation studies to fully exercise the model.

3. The pre-peak damage evolution is dominated by matrix cracks and fiber damage in the $0°$ plies. Post-peak, delaminations are always observed. Based on the analysis results, it is observed that the Hard and Quasi layups collapse as a result of fiber compression damage (kinking) in the $0°$ plies, whereas the Soft laminate collapses due to delamination and sublaminate buckling. Increased fidelity of test measurements, especially near the peak load, is needed to experimentally determine the governing failure mode. Also, test and analysis efforts directed at enhancing understanding of the interaction between fiber kinking and delamination will help improve capability for future OHC models.

4. Overlaying the measured and predicted damage states at 70% and 90% load levels served to highlight the differences between the test and analysis damage states. It was noteworthy that in all cases, only partial agreement was found. Quantitatively accurate agreement in terms of damage states was not possible to achieve.

5. Sensitivity studies show that thermal residual stresses and difficult-to-measure material property inputs can have a significant influence on the results. Fiber compressive fracture toughness obtained following [34], which yields a value roughly twice that obtained from other methods, appears to be appropriate for use in the current modeling approach. The sensitivity study revealed a spurious damage pattern in one case, which highlights the need to validate models across the anticipated input parameter space–an expensive undertaking for complex PDFA models.

References

1. Waas, A. M., Babcock Jr., C. D., and Knauss, W. G., "An experimental study of compression failure of fibrous laminated composites in the presence of stress gradients," *International Journal of Solids and Structures*, Vol. 26, No. 9–10, 1990, pp. 1071–1098.

2. Soutis, C. and Fleck, N., "Static compression failure of carbon fibre T800/924C composite plate with a single hole," *Journal of Composite Materials*, Vol. 24, 1990, pp. 536–558.

3. Lessard, L. B. and Chang, F.-K., "Damage tolerance of laminated composites containing an open hole and subjected to compressive loadings: Part II—Experiment," *Journal of Composite Materials*, Vol. 25, Jul. 1991, pp. 44–64.

4. Soutis, C., "Damage tolerance of open-hole CFRP laminates loaded in compression," *Composites Engineering*, Vol. 4, No. 3, Jan. 1994, pp. 317–327.

5. Suemasu, H., Takahashi, H., and Ishikawa, T., "On failure mechanisms of composite laminates with an open hole subjected to compressive load," *Composites Science and Technology*, Vol. 66, No. 5, May 2006, pp. 634–641.

6. Suemasu, H., Naito, Y., Gozu, K., and Aoki, Y., "Damage initiation and growth in composite laminates during open hole compression tests," *Advanced Composite Materials*, Vol. 21, No. 3, Jun. 2012, pp. 209–220.

7. Lee, J. and Soutis, C., "A study on the compressive strength of thick carbon fibre–epoxy laminates," *Composites Science and Technology*, Vol. 67, No. 10, Aug. 2007, pp. 2015–2026.

8. Xu, X., Paul, A., Sun, X., and Wisnom, M. R., "An experimental study of scaling effects in notched quasi-isotropic carbon/epoxy laminates under compressive loads," *Composites Part A: Applied Science and Manufacturing*, Vol. 137, Oct. 2020, pp. 106029.

9. Leopold, C., Schütt, M., Liebig, W. V., Philipkowski, T., Kürten, J., Schulte, K., and Fiedler, B., "Compression fracture of CFRP laminates containing stress intensifications," *Materials*, Vol. 10, No. 99, Sep. 2017, pp. 1039.

10. Iarve, E. V., Mollenhauer, D., and Kim, R., "Theoretical and experimental investigation of stress redistribution in open hole composite laminates due to damage accumulation," *Composites Part A: Applied Science and Manufacturing*, Vol. 36, No. 2, Feb. 2005, pp. 163–171.

11. Lee, J. and Soutis, C., "Measuring the notched compressive strength of composite laminates: Specimen size effects," *Composites Science and Technology*, Vol. 68, No. 12, Sep. 2008, pp. 2359–2366.

12. Davidson, P., Pineda, E., Heinrich, C., and Waas, A., "A unified model for predicting the open hole tensile and compressive strengths of composite laminates

for aerospace applications," *54th AIAA/ASME/ASCE/AHS/ASC Structures, Structural Dynamics, and Materials Conference*, Boston, MA, Apr. 2013.

13. Su, Z. C., Tay, T. E., Ridha, M., and Chen, B. Y., "Progressive damage modeling of open-hole composite laminates under compression," *Composite Structures*, Vol. 122, Apr. 2015, pp. 507–517.

14. Zhi, J. and Tay, T.-E., "Interrogating failure mechanisms of notched composites through a discrete crack modeling approach," *Composites Science and Technology*, Vol. 196, Aug. 2020, pp. 108203.

15. Engelstad, S. P. and Clay, S. B., "Comparison of composite damage growth tools for static behavior of notched composite laminates," *Journal of Composite Materials*, Vol. 51, No. 10, 2017, pp. 1493–1524.

16. Kaddour, A. S., Hinton, M. J., Smith, P. A., and Li, S., "A comparison between the predictive capability of matrix cracking, damage and failure criteria for fibre reinforced composite laminates: Part A of the third world-wide failure exercise," *Journal of Composite Materials*, Vol. 47, No. 20-21, Sep. 2013, pp. 2749–2779.

17. Wanthal, S., Schaefer, J. D., Justusson, B., Hyder, I., Englestad, S., and Rose, C., "Verification and validation process for progressive damage and failure analysis methods in the NASA Advanced Composites Consortium," *American Society for Composites 32nd Technical Conference*, West Lafayette, Indiana, Oct. 2017.

18. Leone Jr., F. A., Dávila, C. G., Mabson, G. E., Ramnath, M., and Hyder, I., "Fracture-based mesh size requirements for matrix cracks in continuum damage mechanics models," *58th AIAA/ASCE/AHS/ASC Structures, Structural Dynamics, and Materials Conference*, AIAA SciTech Forum, Grapevine, TX, Jan. 2017.

19. Leone Jr., F. A., Ramnath, M., Hyder, I., Wanthal, S., Schaefer, J. D., and Mabson, G. E., "Benchmarking mixed mode failure in progressive damage and failure analysis methods," *American Society for Composites 33rd Technical Conference*, Seattle, WA, Sep. 2018.

20. Justusson, B., Hyder, I., Boyd, S., and Leone Jr., F. A., "Quantification of error associated with using misaligned meshes in continuum damage mechanics material models for matrix crack growth predictions in composites," *American Society for Composites 33rd Technical Conference*, Seattle, WA, Sep. 2018.

21. Song, K., Leone, F. A., and Rose, C. A., "Continuum damage mechanics models for the analysis of progressive damage in cross-ply and quasi-isotropic panels subjected to static indentation," *59th AIAA/ASCE/AHS/ASC Structures, Structural Dynamics, and Materials Conference*, AIAA SciTech Forum, Kissimmee, FL, Jan. 2018.

22. Hyder, I., Leone Jr., F. A., Justusson, B., Schaefer, J. D., Bergan, A. C., and Wanthal, S., "Implementation of a matrix crack spacing parameter in a continuum damage mechanics finite element model," *American Society for Composites 33rd Technical Conference*, Seattle, Washington, Sep. 2018.

23. Leone Jr., F. A., Song, K., Johnston, W. M., Rose, C. A., Jackson, W. C., and Dávila, C. G., "Test/analysis correlation of damage states in stiffened post-buckled validation building block specimens," *American Society for Composites 34th Technical Conference*, Atlanta, GA, Sep. 2019.

24. Selvarathinam, A. S., Carvalho, N. V. D., Seshadri, B. R., and Johnson, V., "Validation of floating node method using three-point bend doubler under quasi-static loading," *60th AIAA/ASCE/AHS/ASC Structures, Structural Dynamics, and Materials Conference*, AIAA SciTech Forum, San Diego, CA, Jan. 2019.

25. Leone, F. A., Song, K., Rose, C., and Jackson, W., "Progressive damage analysis of post-buckled stiffened panels under static compressive loading," *61st AIAA/ASCE/AHS/ASC Structures, Structural Dynamics, and Materials Conference*, AIAA SciTech Forum, Orlando, FL, Jan. 2020.

26. Action, J., Leone, F. A., and Carvalho, N. V. D., "Progressive damage analysis of a multi-stringer post-buckled panel," *61st AIAA/ASCE/AHS/ASC Structures, Structural Dynamics, and Materials Conference*, AIAA Scitech Forum, Orlando, FL, Jan. 2020.

27. Leone, F., Bergan, A. C., and Dávila, C. G., "CompDam - Deformation Gradient Decomposition (DGD) v2.5.0," 2020, https://github.com/nasa/CompDam_DGD.

28. Leone Jr., F. A., "Deformation gradient tensor decomposition for representing matrix cracks in fiber-reinforced materials," *Composites Part A: Applied Science and Manufacturing*, Vol. 76, Sep. 2015, pp. 334–341.

29. Wisnom, M. R., Hallett, S. R., and Soutis, C., "Scaling effects in notched composites," *Journal of Composite Materials*, Vol. 44, No. 2, Jan. 2010, pp. 195–210.

30. "ASTM Standard D6484. Standard test method for open-hole compressive strength of polymer matrix composite laminates," *Annual Book of ASTM Standards*, ASTM Int., 2014.

31. Action, J. and Palliyaguru, U. R., "Testing of a multi-stringer post-buckled panel," *61st AIAA/ASCE/AHS/ASC Structures, Structural Dynamics, and Materials Conference*, AIAA Scitech Forum, Orlando, FL, Jan. 2020.

32. Simulia, *Abaqus Analysis User's Guide. Version 2019*, 2019.

33. Clarkson, E., "Hexcel 8552 IM7 unidirectional prepreg 190 GSM & 35% RC qualification statistical analysis," Tech. Rep. NCP-RP-2009-028, NIAR, Jun. 2011.

34. Catalanotti, G., Xavier, J., and Camanho, P., "Measurement of the compressive crack resistance curve of composites using the size effect law," *Composites Part A: Applied Science and Manufacturing*, Vol. 56, 2014, pp. 300–307.

35. Dávila, C. G., Rose, C. A., and Camanho, P. P., "A procedure for superposing linear cohesive laws to represent multiple damage mechanisms in the fracture of composites," *International Journal of Fracture*, Vol. 158, No. 2, Aug. 2009, pp. 211–223.

36. Mims, A., *Calibration of bilinear softening cohesive law for modeling fiber compressive failure*, Master's thesis, San Diego State University, 2019.

37. Van Paepegem, W., De Baere, I., and Degrieck, J., "Modelling the nonlinear shear stress–strain response of glass fibre-reinforced composites. Part I: Experimental results," *Composites Science and Technology*, Vol. 66, No. 10, Aug. 2006, pp. 1455–1464.

38. Dávila, C. G. and Camanho, P. P., "Failure criteria for FRP laminates in plane stress," Tech. rep., NASA/TM-2003-212663, NASA Langley Research Center, Nov. 2003.

39. Jones, R. M., *Mechanics of Composite Materials*, Taylor and Francis Group, 1999.

40. Laurin, F., Paulmier, P., and Irisarri, F. X., "Determination of the longitudinal compressive strength of a CFRP ply through a tensile test on a laminate," *Composites Part A: Applied Science and Manufacturing*, Vol. 113, Oct. 2018, pp. 209–219.

41. Camanho, P., Maimí, P., and Dávila, C. G., "Prediction of size effects in notched laminates using continuum damage mechanics," *Composites Science and Technology*, Vol. 67, No. 13, Oct. 2007, pp. 2715–2727.

42. Catalanotti, G., Camanho, P., Xavier, J., Dávila, C. G., and Marques, A., "Measurement of resistance curves in the longitudinal failure of composites using digital image correlation," *Composites Science and Technology*, Vol. 70, No. 13, Nov. 2010, pp. 1986–1993.

43. Laffan, M. J., Pinho, S. T., Robinson, P., Iannucci, L., and McMillan, A. J., "Measurement of the fracture toughness associated with the longitudinal fibre compressive failure mode of laminated composites," *Composites Part A: Applied Science and Manufacturing*, Vol. 43, No. 11, Nov. 2012, pp. 1930–1938.

44. Wind, J. L., Waas, A. M., and Jensen, H. M., "Initiation of failure at notches in unidirectional fiber composites," *Composite Structures*, Vol. 122, Apr. 2015, pp. 51–56.

REPORT DOCUMENTATION PAGE

1. REPORT DATE (DD-MM-YYYY)
01-11-2020

2. REPORT TYPE
Technical Memorandum

3. DATES COVERED (From - To)

4. TITLE AND SUBTITLE
Analysis of Open Hole Compression Specimens Using the CompDam Continuum Damage Mechanics Model

5a. CONTRACT NUMBER

5b. GRANT NUMBER

5c. PROGRAM ELEMENT NUMBER

6. AUTHOR(S)
Bergan, Andrew C. and Murphy, Sara J. and Miles, Lillian F.

5d. PROJECT NUMBER

5e. TASK NUMBER

5f. WORK UNIT NUMBER
826611.04.07.01

7. PERFORMING ORGANIZATION NAME(S) AND ADDRESS(ES)
NASA Langley Research Center
Hampton, Virginia 23681-2199

8. PERFORMING ORGANIZATION REPORT NUMBER

9. SPONSORING/MONITORING AGENCY NAME(S) AND ADDRESS(ES)
National Aeronautics and Space Administration
Washington, DC 20546-0001

10. SPONSOR/MONITOR'S ACRONYM(S)
NASA

11. SPONSOR/MONITOR'S REPORT NUMBER(S)
NASA/TM–20205009618

12. DISTRIBUTION/AVAILABILITY STATEMENT
Unclassified-Unlimited
Subject Category 24
Availability: NASA STI Program (757) 864-9658

13. SUPPLEMENTARY NOTES

14. ABSTRACT This report documents a validation study on the standard Open Hole Compression (OHC) laminate test specimen conducted as part of the NASA Advanced Composites Project (ACP). Tests were conducted on OHC specimens with hard, quasi-isotropic, and soft layups using digital image correlation and X-Ray computed tomography to capture the structural response and damage evolution. Progressive damage models were constructed for use with the CompDam continuum damage mechanics code following the best practices established during the ACP. Detailed interrogation of the analysis results and comparison with experimental measurements provide a basis for assessing the capability of the modeling approach for OHC. The structural response is found to be captured well, with strengths predicted within 3\% of the experimental values for hard and quasi-isotropic laminates. In the soft laminate, the model predicts failure to be more brittle than the nonlinear, ductile response that was measured. Damage states extracted from the models at the same load level as test measurements are overlaid to show directly the similarities and differences between test and analysis results. Studying the damage evolution predicted by the analysis reveals that the failure process is a competition between fiber damage and delamination/sub-laminate buckling, with fiber damage dominating the collapse in the hard laminate and sub-laminate buckling governing in the soft laminate. Finally, a series of parametric studies varying numerical solution parameters (mesh size, mass scaling) and physical properties (fiber direction compressive strength and toughness) reveal sensitivities and deficiencies of the model. To the authors' knowledge, this study is the first for OHC specimens to include detailed evaluation of damage mode interactions, direct overlay of predicted and measured damage states, and sensitivity of the predicted results to difficult-to-measure fiber direction material properties.

15. SUBJECT TERMS

16. SECURITY CLASSIFICATION OF:

a. REPORT	b. ABSTRACT	c. THIS PAGE
U	U	U

17. LIMITATION OF ABSTRACT
UU

18. NUMBER OF PAGES
58

19a. NAME OF RESPONSIBLE PERSON
STI Information Desk (help@sti.nasa.gov)

19b. TELEPHONE NUMBER (Include area code)
(757) 864-9658